

1
2
3
4
5
6
7
8

A Novel Definition of Climate State Using Kalman Filtering and Application to Thresholds

J. Matthew Nicklas,^a Baylor Fox-Kemper,^a Charles Lawrence.^a

^a *Brown University, Providence, Rhode Island.*

Corresponding author: J. Matthew Nicklas, john_nicklas@brown.edu

9

ABSTRACT

10 Herein we present the Energy Balance Model – Kalman Filter (EBM-Kalman), a hybrid
11 model of the global mean surface temperature (GMST), which combines a theoretical energy
12 balance equation based in Earth science literature and a statistical extended Kalman Filter
13 incorporating observed and/or climate model simulated GMST data. This synthesis is
14 possible because climate models and historical temperatures follow easily representable
15 normal distributions due to dynamic instability. A Kalman filter is a powerful, fast tool which
16 assumes normal distributions at each time point, and combines a forward projection given by
17 the energy balance equation with the measured GMST in a weighted average. This model
18 generates an estimate of the 30-year time-averaged climate state but can do so
19 instantaneously: without a lag time of 15 years. It can also determine reasonable probabilities
20 that the climate has crossed a particular threshold or expand the statistical spread of a few
21 computationally intensive simulations of the global climate to estimate an entire ensemble.

22

23

SIGNIFICANCE STATEMENT

24 The overall shape of the Earth's historical climate over the past 150 years can be
25 explained by thermal/light physics equations involving ~12 constants, atmospheric CO₂, and
26 volcanic eruptions. Global mean surface temperature measurements vary around this climate
27 state within a consistent distribution. These two observations allowed us to construct a simple
28 model that can estimate Earth's current climate and aid in policy discussions of climate
29 thresholds.

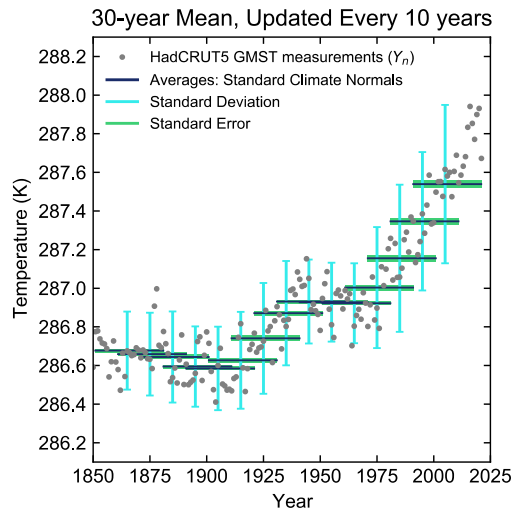
30

31 **1. Introduction**

32 What is the uncertainty in Earth's climate? From a measurement standpoint, this issue was
33 resolved many decades ago. The instantaneous measurement of global mean surface
34 temperature (GMST) is currently performed with average precision of 0.05°C (max 0.10°C)
35 via arrays of infrared-sensing satellites and ground stations (Susskind, Schmidt et al. 2019),
36 both these datasets extend back to 1981 (Merchant, Embury et al. 2019), and the cyclical
37 yearly fluctuation (due to the lopsided distribution of Earth's land mass) is easy to smooth
38 with a running annual average. However, this GMST is still a noisy variable, subject to such
39 factors as El Nino events in the tropical Pacific that typically oscillate with a period of 2-7

40 years (Hu and Fedorov 2017) and volcanic eruptions that may randomly perturb the climate
41 for 1-2 years (Soden, Wetherald et al. 2002). There are also complexities arising from sparse
42 and inconsistently calibrated historical data and paleoproxy interpretations as the record is
43 extended backward in time (Carré, Sachs et al. 2012; Emile-Geay, McKay et al. 2017;
44 Kaufman, McKay et al. 2020; McClelland, Halevy et al. 2021). Internal variability dominates
45 many climate quantities in the short-term and is much larger than many climate forcing
46 signals, both in climate simulations and reality. (Kirtman, Power et al. 2013; Marotzke and
47 Forster 2015; Gulev, Thorne et al. 2021; Lee, Marotzke et al. 2021) Variables other than
48 GMST, such as Ocean Heat Content Anomaly where >90% of the anthropogenic energy
49 anomaly is found, reveal that the earth's thermal energy is steadily warming (Gulev et al.
50 2021; Fox-Kemper et al. 2021), but some smoothing or filtering is required to uncover
51 anthropogenic climate change in the GMST record.

52 In 1935 the World Meteorological Association began reporting the "standard climate
53 normal" as discrete averages of the global temperatures measured over an interval of 30 years
54 (\overline{T}_{30} , starting with 1901-1930), precisely to address the detection of climate change over
55 internal variability and measurement uncertainties in the GMST record. (Guttman 1989) The
56 World Meteorological Association later began updating the 30-year interval every 10 years.
57 A 30-year window is sufficiently long to minimize most fluctuations from climate variability
58 modes (such as El Nino) or short-term forcings such as single volcanoes or solar cycles. This
59 averaged global climate is depicted in Figure 1, and it can be easily updated yearly by a
60 running average rather than every decade (Supp. Fig. 1b). While standard climate normals
61 and running averages are straightforward and widely accepted definitions, these metrics
62 reflect the average climate state centered on 15 years ago, and most of the variability
63 contained within recent 30-year periods reflect the anthropogenic warming trend, rather than
64 the variability that the 30-year "standard climate normal" was designed to smooth out.



65

66 Fig. 1: Illustration of Standard Climate Normals as applied to the HadCRUT5 temperature
 67 dataset. (Morice, Kennedy et al. 2021) Note the standard deviation widens considerably due
 68 to the considerable increase in temperatures over the 30-year averaging windows in recent
 69 decades.

70

71 Considering climate policy goals, which often frame decision-making to avoid a
 72 particular threshold (e.g., 1.5°C or 2°C above pre-industrial conditions), a 30-year mean
 73 implies some difficulty in determining exactly when or if a threshold is crossed (Lee et al.
 74 2021). Tools for assessing the probability that the threshold has been crossed in the past year
 75 will be increasingly useful in as these policy targets approach. Relatedly, magnitudes and
 76 uncertainty ranges of climate warming must hitherto be attached to specific averaging
 77 windows, e.g., “GMST increased by 0.85 [0.69 to 0.95] °C between 1850–1900 and 1995–
 78 2014 and by 1.09 [0.95 to 1.20] °C between 1850–1900 and 2011–2020.” (Gulev, Thorne et
 79 al. 2021). Our method describes the past year’s climate system temperature, with
 80 uncertainties reflecting the internal variability consistent with the standard 30-year mean.

81 Mathematically, averaging filters out high-frequency signals that reflect year-to-year
 82 variations in global weather, as do other approaches. While moving average filters are good
 83 at preserving sudden large sustained changes (such as the anthropogenic change beginning in
 84 the mid-1960s in Fig. 1) while removing random noise, other filters or smoothers are better-
 85 suited to removing frequencies above a particular cutoff. (Smith 2003) For instance, the
 86 Butterworth Smoother has been applied to this global surface temperature time series (Supp.
 87 Fig. 1d). (Mann 2008) A sophisticated modification of time-averaging allows for adaptive

88 periods of multiyear averages, known as the optimal climate normal (OCN). (Livezey,
89 Vinnikov et al. 2007). This method utilizes trendlines to determine the number of years to
90 include in each average, with steeper slopes resulting in shorter averaging periods (Supp. Fig.
91 1c). This OCN is a trade-off: the standard deviation is reduced compared to the standard
92 climate normals in the latter 20th century, whereas the small size of recent averaging periods
93 causes the standard error to increase. Other techniques directly use trendlines. The trendline
94 intervals may be chosen somewhat arbitrarily, say before and after 1975 in the "hinge shape".
95 (Livezey, Vinnikov et al. 2007) Alternatively, Bayesian sequential change point detection
96 may be used to find a probability distribution of the best trendline intervals (Ruggieri and
97 Antonellis 2016) This method takes the climate state as the average of all potential trendlines.
98 (Supp. Fig. 2)

99 However, climate studies often instead investigate the climate system within coupled
100 climate or earth system models ("coupled" refers to the interaction between multiple sub-
101 models, principally the atmosphere and ocean; (Meehl, Moss et al. 2014)). Typically, these
102 simulations are forced using inputs of historical records and a range of scenarios of future
103 projections (including CO₂ emissions, other pollutants, and land use; Lee et al. 2021). Subtle
104 variation of initial conditions can produce a population of identically-forced simulations that
105 through the chaotic nature of weather explore the whole span of the climate system's range of
106 outcomes consistent with that climate forcing, such as for the CESM2 Large Ensemble
107 (Rodgers, Lee et al. 2021), abbreviated here as LENS2. Unfortunately, each ensemble
108 member is computationally expensive, and does not accurately or transparently reflect the
109 real climate system.

110 Therefore, we have created a model that has both an energy-balance difference equation
111 intended to capture the underlying physics and a statistical observation equation that brings in
112 the available data hybrid physical model-statistical filter. Our model is one example of data-
113 driven climate emulators (Forster, Storelvmo et al. 2021), which by construction contains
114 specific benefits inherited from its chosen constituent models. Our simple iterative energy-
115 balance model contains the major driving physics of the climate system with just 12
116 coefficients (of which 5 are reducible) and has good skill at predicting the GMST despite
117 being "blind" to all measurements (i.e., a "forward" model in numerical weather prediction
118 terminology). The statistical component is an extended Kalman Filter, which allows for
119 incorporation of current measurements to "course-correct" under a well-understood
120 mathematical framework. Hybridizing these two models yields statistical distributions of

121 uncertainty due to internal variability regarding the current climate state. In other words, it is
 122 a simplified data assimilation tool. This combined model can project into the future,
 123 transparently driven by climate forcers: CO₂ and volcanic dust. Furthermore, its internal
 124 uncertainty approximates the spread of simulation model ensembles (e.g., LENS2). Of
 125 course, large ensembles also predict regional variability and changes to components such as
 126 subsurface oceans, sea ice, clouds, etc., while this model predicts only GMST.

127

128 **2. Methods**

129 *a. Energy-Balance Model*

130 The energy-balance model is constructed by envisioning a uniform planet and capturing
 131 the principal atmospheric and surface energy fluxes (Budyko 1969; Sellers 1969). This model
 132 is "blind" with respect to current GMST measurements, and is inspired by the work of other
 133 energy-budget models illustrating quantitative skill (Hu and Fedorov 2017; Kravitz, Rasch et
 134 al. 2018).

$$135 \quad \Delta \text{Energy} = \phi_{\text{SW}}(\text{in}) - \phi_{\text{LW}}(\text{out}) \quad (1)$$

$$136 \quad \frac{T_{n+1} - T_n}{k} C_{\text{heat}} = G_0 * \tilde{d}_n * f_{\alpha A}(T_n) * f_{\alpha S}(T_n) - j^* * \tilde{g}_n * f_{H_2O}(T_n) \quad (2)$$

137 The time unit k is 1 year, matching the time step of this iterative difference equation
 138 model. For simplicity, n is taken as the calendar year (e.g., 2000). On the right side of the
 139 equation, both the shortwave radiative flux and longwave radiative flux take the same form:
 140 (source G_0, j^*) * (prescribed attenuation: \tilde{d}_n, \tilde{g}_n) * (feedback attenuation: $f_i(T_n)$). The heat
 141 capacity of the whole climate system and land mass on a yearly time scale, C_{heat} , is known
 142 with the least precision: reported values are $17 \pm 7 \text{ W (year) m}^{-2} \text{ K}^{-1}$, (Schwartz, 2007). G_0 is
 143 the extraterrestrial irradiance at 340 W/m^2 , \tilde{d}_n is the prescribed shortwave light attenuation
 144 due to volcanic dust, $f_{\alpha A}(T_n)$ is the additional atmospheric shortwave attenuation due to cloud
 145 albedo, while $f_{\alpha S}(T_n)$ is the surface shortwave attenuation due to ground albedo. The ideal
 146 black body radiation is $j^* = \sigma_{\text{sf}} T_n^4$ (also known as Planck feedback), \tilde{g}_n is the prescribed
 147 longwave attenuation due to CO₂ scaled to include other greenhouse gasses, and $f_{H_2O}(T_n)$ is
 148 the additional atmospheric longwave attenuation due to water vapor and other gasses
 149 parameterized as a function of GMST. Several of these terms were defined to satisfy the
 150 constraints of the climate feedbacks presented in the IPCC's AR6 (Forster et al. 2021;
 151 particularly Table 7.10), and all coefficients were based on literature values (full derivation in

152 Appendix A). The model also assumes a prehistorical (1850) GMST of 286.7K (13.55°C),
 153 which allows the 1960-1990 "standard climate normal" to fall within the range given by
 154 Jones and Harpham (2013). The two albedo feedbacks are expressed relative to 287.5K, the
 155 temperature in 2002.

156 Overall, this yields a blind (forward) energy-balance model (see the orange dashed line in
 157 Figure 2) with 7 irreducible, non-integer coefficients and good skill at predicting the GMST
 158 with an $R^2 = 0.88$ in describing the HadCrut5 GMST timeseries (Morice, Kennedy et al.
 159 2021). With only minor modifications, this method could be used with *multiple* annual
 160 temperature reconstructions at the same time (e.g. GISTEMP (Lenssen, Schmidt et al. 2019)),
 161 considering each as only an estimate of the true GMST. (Willner, Chang et al. 1977)

$$162 \quad T_{n+1} = T_n + \frac{137.7m}{AOD_n + 9.73m} \left(1 + \frac{T_n - 287.5K}{687.1K}\right) \left(1 + \frac{T_n - 287.5K}{572.6K}\right) \\
 163 \quad - \left(\frac{T_n}{274.9K}\right)^{2.385} \log_{10} \left(\frac{1.893 * 10^{15} \text{ppm}}{[CO_2]_n}\right) = F(T_n; [CO_2]_n, AOD_n) \quad (3)$$

$$164 \quad \frac{\partial T_{n+1}}{\partial T_n} = 1 + \frac{0.4407m}{AOD_n + 9.73m} \left(1 + \frac{T_n - 287.5K}{629.9K}\right) \\
 165 \quad - \left(\frac{T_n}{8464.K}\right)^{1.385} \log_{10} \left(\frac{1.893 * 10^{15} \text{ppm}}{[CO_2]_n}\right) = \frac{\partial F(T_n; [CO_2]_n, AOD_n)}{\partial T_n} \quad (4)$$

166 This function F and the partial derivative of F will become critical parts of the Kalman
 167 filter: (6-8) below.

168 *b. EBM-Kalman Filter: A Weighted Average of Energy Balance and Measurements*

169 While similar algorithms were developed in the 1880s by Thorvald Nicolai Thiele
 170 (Lauritzen 1981; Lauritzen and Thiele 2002), Kalman filtering rose to prominence due to its
 171 use in the Apollo navigation computer as proposed by Ruslan Stratonovich (1959; 1960),
 172 Peter Swerling (1959), Rudolf E. Kálmán (1960), Richard S. Bucy (1961), and implemented
 173 by Stanley Schmidt (1981). Versions of this statistical filter are universally used in aerospace
 174 guidance systems, as well as in a variety of other scientific fields. (Grewal and Andrews
 175 2001) They are also often used in aspects of numerical weather prediction (Annan,
 176 Hargreaves et al. 2005), although they are ineffective as the sole data assimilation tool for
 177 weather (Bouttier 1996). The Kalman filter can be applied to most situations in which there
 178 are noisy measurements of a system with known underlying dynamics.

179 In-depth derivations and tutorials for constructing Kalman filters have been published
 180 elsewhere (Miller 1996; Lacey 1998; Särkkä 2013; Benhamou 2018; Youngjoo and

181 Hyochoong 2018; Ogorek 2019), although there is no standard symbol convention. Here we
182 provide a basic intuition, using the seminal example of the Apollo spacecraft. Initially, there
183 is some estimated *state vector* (acceleration, velocity, and position vectors) of the craft $\hat{\mathbf{x}}_{n-1}$
184 and a Gaussian uncertainty envelope around this vector defined by a *state covariance matrix*
185 \mathbf{P}_{n-1} . These can be projected a priori into the future using a *dynamic model matrix* Φ (for a
186 spacecraft this is from physics, for our climate system this is extended to the function F (7),
187 the energy balance model (3)), and the projected covariance enlarges by an additional
188 assumed *model covariance* \mathbf{Q} , yielding $\mathbf{P}_{n|n-1}$ (8). Now a *measurement vector* \mathbf{y}_n is considered
189 (9). The probabilistic range of discrepancies between $\Phi\hat{\mathbf{x}}_{n-1}$ and \mathbf{y}_n is given by the *innovation*
190 *covariance matrix* \mathbf{S}_n , which is the sum of $\mathbf{P}_{n|n-1}$ and an assumed *measurement covariance* \mathbf{R}
191 (10). The *a posteriori estimate* for the state $\hat{\mathbf{x}}_n$ is found by taking a weighted average of $\Phi\hat{\mathbf{x}}_{n-1}$
192 and \mathbf{y}_n (12), with the weight on \mathbf{y}_n given by $\mathbf{P}_{n|n-1}(\mathbf{S}_n)^{-1}$, a product known as the *Kalman gain*
193 (11). To reflect the greater certainty in the state vector because of this correction, \mathbf{P}_n , the *a*
194 *posteriori covariance matrix*, is $\mathbf{P}_{n|n-1}$ shrunk by a factor of (\mathbf{I} minus the Kalman gain (13)).
195 To summarize within the context of Bayesian probability, the *prior distribution* is given by
196 projecting $\mathcal{N}(\hat{\mathbf{x}}_{n-1}, \mathbf{P}_{n-1})$ into the future using Φ , which is multiplied by the support of \mathbf{y}_n to
197 give a *posterior distribution* $\mathcal{N}(\hat{\mathbf{x}}_n, \mathbf{P}_n)$.

198 If \mathbf{y}_n is an indirect measurement of the state vector \mathbf{x}_n (for instance Apollo's
199 accelerometers, or GMST approximated by a set of different measurements across the globe),
200 this necessitates an emission / observation matrix \mathbf{H} , further complicating the above
201 procedure. For this application to the global climate system, all terms are scalars and the
202 emission matrix $\mathbf{H} = \mathbf{I} = 1$, so we use italicized notation to indicate this case.

$$203 \quad \Phi_n = \left. \frac{\partial F(x; u_n)}{\partial x} \right|_{x=\hat{x}_{n-1}} \quad \text{linearization at timepoint } n \quad (5)$$

$$204 \quad \begin{cases} x_n = F(x_{n-1}; u_n) + w_n \\ y_n = x_n + v_n \end{cases} \quad \begin{array}{l} \text{dynamic model, error: } Q = E[w_n^2] \\ \text{measurements, error: } R = E[v_n^2] \end{array} \quad (6)$$

$$205 \quad \hat{x}_{n|n-1} = F(\hat{x}_{n-1}; u_n) \quad \text{a priori estimated state projection} \quad (7)$$

$$206 \quad \mathbf{P}_{n|n-1} = \Phi_n^2 \mathbf{P}_{n-1} + \mathbf{Q} \quad \text{a priori state variance projection} \quad (8)$$

$$207 \quad c_n = y_n - \hat{x}_{n|n-1} \quad \text{innovation residual} \quad (9)$$

$$208 \quad \mathbf{S}_n = \mathbf{P}_{n|n-1} + \mathbf{R} \quad \text{innovation covariance} \quad (10)$$

$$209 \quad \mathbf{K}_n = \mathbf{P}_{n|n-1} / \mathbf{S}_n \quad \text{Kalman gain} \quad (11)$$

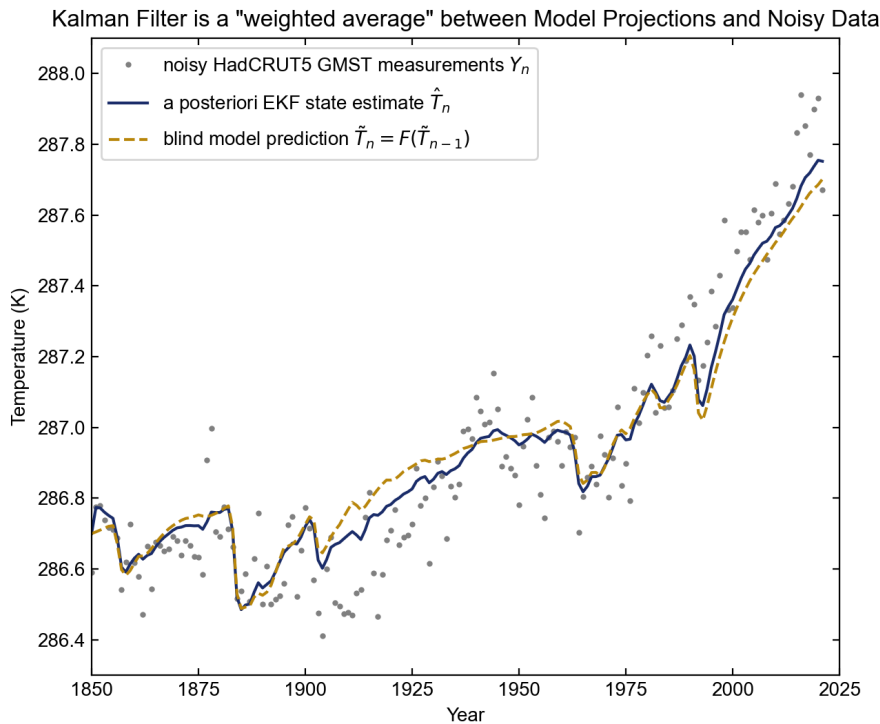
$$210 \quad \hat{x}_n = \hat{x}_{n|n-1} + \mathbf{K}_n c_n \quad \text{a posteriori estimated state} \quad (12)$$

211
$$P_n = (1 - K_n) P_{n|n-1}$$
 a posteriori state covariance (13)

212 Returning to the original climate state context of this paper, we are concerned with a
 213 one-dimensional GMST, so the equations are for simple scalars rather than matrices and
 214 vectors. Here, we take the abstract unknown state x_n to be climate temperature, particularly an
 215 underlying GMST capturing only the climate state T_n and not annual weather-pattern related
 216 variability in GMST. The noisy measurements Y_n are the yearly time series of GMST
 217 measurements, and \hat{T}_n is the estimate of the unknown climate state, both expressed in units of
 218 K. The energy-balance model F (3) governing \hat{T}_n is nonlinear (with T^2 and $T^{2.385}$ terms due to
 219 albedo and Planck feedbacks), which necessitates an extended Kalman filter (EKF): the a
 220 priori estimated state projection is given by (7) above and Φ_n for the a priori state covariance
 221 (8) projection is a time-varying linearization (5). This energy-conserving difference equation
 222 resembles using a first-order Taylor series approximation of a differential energy-balance
 223 model (if discretization errors are considered part of the tendency), or the integral form of a
 224 conservative discretization in time (if fluxes on the right side are taken as a model for their
 225 time-integrated value), and the Kalman Filter re-approximates a climate state underlying the
 226 GMST at every time step. Conveniently, because the derivative of the energy-balance
 227 equation does not change significantly over the relevant range of temperatures (286K -
 228 289K), more complex extensions of the Kalman filter, particularly the Unscented Kalman
 229 Filter (Julier and Uhlmann 1997; Wan and Van Der Merwe 2000) is not necessary (see
 230 Appendix B).

231 In summary, the extended Kalman filter projects forward one year into the future
 232 based on the unbalanced fluxes of the energy balance model equation, and then takes a
 233 weighted average of this projection with the annual GMST measurement (the data
 234 assimilation increment). Thus, even though the EBM conserves energy (by construction), the
 235 combined EBM-Kalman Filter does not, unlike other alternative data assimilation approaches
 236 (e.g., (Wunsch and Heimbach 2007)). The state estimates from this EBM-Kalman Filter (in
 237 navy blue in Fig. 2) almost always lie between the blind EBM (in dashed orange in Fig. 2)
 238 and the annual GMST measurements (scattered gray dots in Fig. 2). It is possible for the
 239 EBM-Kalman Filtered state estimates to escape these bounds for a short time, for instance if a
 240 series of colder years shift the EBM-Kalman Filtered state estimate below the blind EBM,
 241 and then the next GMST measurement is slightly warmer than the blind EBM (e.g., from
 242 1937 to 1939 in Fig. 2). While the EBM within the EKF projects warming, this imbalance

243 does not resolve within a single year due to heat capacity and the new observation does not
244 raise the weighted average by much, so the EKF state estimate is colder than both.



245

246 Fig. 2: Depiction of the Kalman Filter's underlying mechanism. The blind energy-balance
247 model prediction is drawn in dashed orange. The Kalman Filter state estimate in navy blue
248 uses these energy-balance dynamics to project from the previous state to the current state.
249 The measured GMST (gray dots - Hadcrut5) pull the Kalman Filter state estimate toward it
250 with a small weight. Note that the $r^2 = 0.88$ is higher for the HadCRUT5 dataset than
251 HadCRUT4 (Morice, Kennedy et al. 2012), but recent time points the measured GMSTs do
252 not match the model quite as nicely and the blind model undershoots. Other researchers may
253 consider that this may justify tweaking the coefficients (eg yet higher β_0 due to stronger
254 short-term forcings).

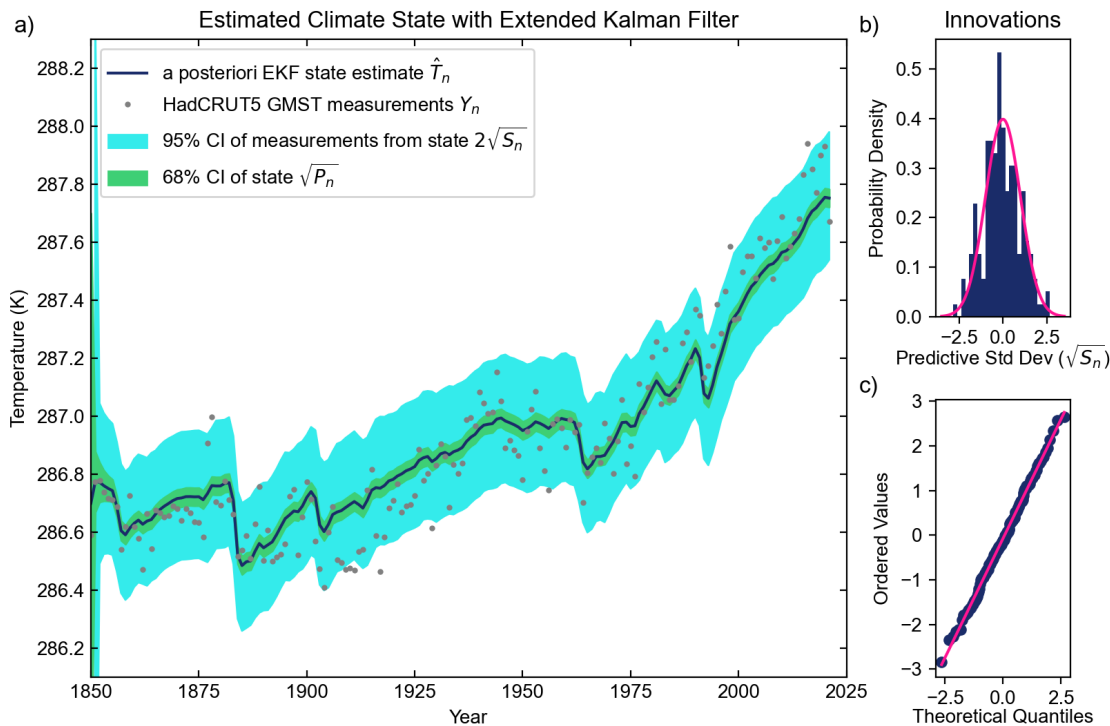
255

256 In this first version of the EKF shown in Fig. 2, we use a measurement uncertainty R
257 in (10) that is constant and based on the HadCRUT5 variance with respect to its 30-year
258 running mean (0.0111 or standard deviation of 0.105K). The climate model uncertainty, Q ,
259 was set to $R/30$ to tie back to the 30-year running average definition of climate state
260 (Guttman 1989). By this simple method, we have tuned the data-assimilating Kalman filter
261 to model the “standard climate normal”.

262

263 **3. Results**

264 *a. The Historical EBM-Kalman Filtered Climate (1850-Present)*



265 Fig. 3: EBM-Kalman Filter and Associated Uncertainties. a) The Kalman Filter state estimate
 266 (navy blue line) is drawn with a $1\sigma = \sqrt{P_n}$ confidence interval (light green area). GMST
 267 measurements are again in gray dots. In light blue, a 2σ confidence interval of the innovation
 268 covariance ($\sqrt{S_n}$) is drawn around the projected state estimate $\hat{T}_{n|n-1}$, which represents a 95%
 269 confidence interval of where the Kalman Filter expects the subsequent year's temperature
 270 measurement to be. After an initial convergence period of about a decade, $\sqrt{P_n}$ converges to
 271 0.0307K and $\sqrt{S_n}$ converges to 0.110K. Note that in 2021 the temperature measurement was
 272 cooler than the climate state predicted, so while the blue temperature forecast window
 273 continues to track warmer with rising CO₂, the state estimate is revised down from the
 274 projected a priori state. b) The deviation between the projected climate state and
 275 measurements, as plotted against the ideal distribution given by the innovation covariance.
 276 The empirical and ideal deviation probability distributions closely match, confirming that the
 277 annual measurements of GMST can be interpreted as Gaussian noise around an underlying
 278 climate state approximating the "standard climate normal" 30-year mean. c) In the qqnorm
 279 plot, the innovation data follows a straight line. This shows good support for the Kalman
 280 filters's assumption of normal residuals.
 281
 282

283 The primary product of this paper is the EBM-Kalman Filtered climate state as
 284 displayed above in Fig. 3a. We emphasize again that all the mathematical constants in the
 285 forward EBM underlying this filter were obtained from published literature values: this is not
 286 an empirical fit to the HadCRUT5 GMST data. Within this Kalman filtered climate, there are

287 two distinct Gaussian distributions relevant to climate science: the uncertainty in the current
288 state, as graphed in light green envelope in Fig. 3a, and the window of possible next-year
289 GMST measurements, as graphed in the light blue envelope in Fig 3a. Further examination of
290 the difference between projected states $\hat{T}_{n|n-1}$ and a posteriori estimated states \hat{T}_n reveals that
291 on an individual year basis, assimilation of the GMST measurement only shifts $\hat{T}_{n|n-1}$ by at
292 most 0.025K, compared with the standard deviation of the adjustment in \tilde{T}_n from the blind,
293 forward model contribution of up to 0.05K per year. However, as demonstrated in Figure 2,
294 repeated small increments of this magnitude by consistently lower or higher than expected
295 GMST measurements can push \hat{T}_n away from \tilde{T}_n by as much as 0.08K over a few years. In
296 net over the entire time series, the measurements have nearly equal warming and cooling
297 contributions to the underlying \hat{T}_n climate state, forming the expected Gaussian distribution
298 as demonstrated in Fig 3B. This reveals that the vast amount of change in the underlying
299 climate state can be explained by the literature-based blind, forward energy-balance model
300 and measurements of greenhouse gas and stratospheric aerosol concentrations, consistent
301 with recent forward-EBM applications (Hu and Fedorov 2017; Kravitz, Rasch et al. 2018).

302

303 *b. Threshold Crossing*

304 An annual measurement is not a measurement of climate change due to the internal
305 variability of the system, and so a single annual temperature above a particular threshold is
306 not a guarantee of the climate state crossing the threshold. We can interpret threshold
307 crossing to reflect when the uncertain climate state (here taken as an estimate of the “standard
308 climate normal”, or 30-year mean temperature) is determined with a given probability to have
309 passed a threshold, or instead could reflect the probability that the possible measurements in
310 the next year will exceed the threshold. This EBM-Kalman Filtered climate product has the
311 convenient ability to generate both GSAT-based probability distributions for whether a
312 threshold has been crossed. Also, both definitions may also be applied to regional climates
313 (with a suitably redefined regional forward model), for instance the former regional threshold
314 crossing definition was investigated by Tebaldi and Knutti (2018).

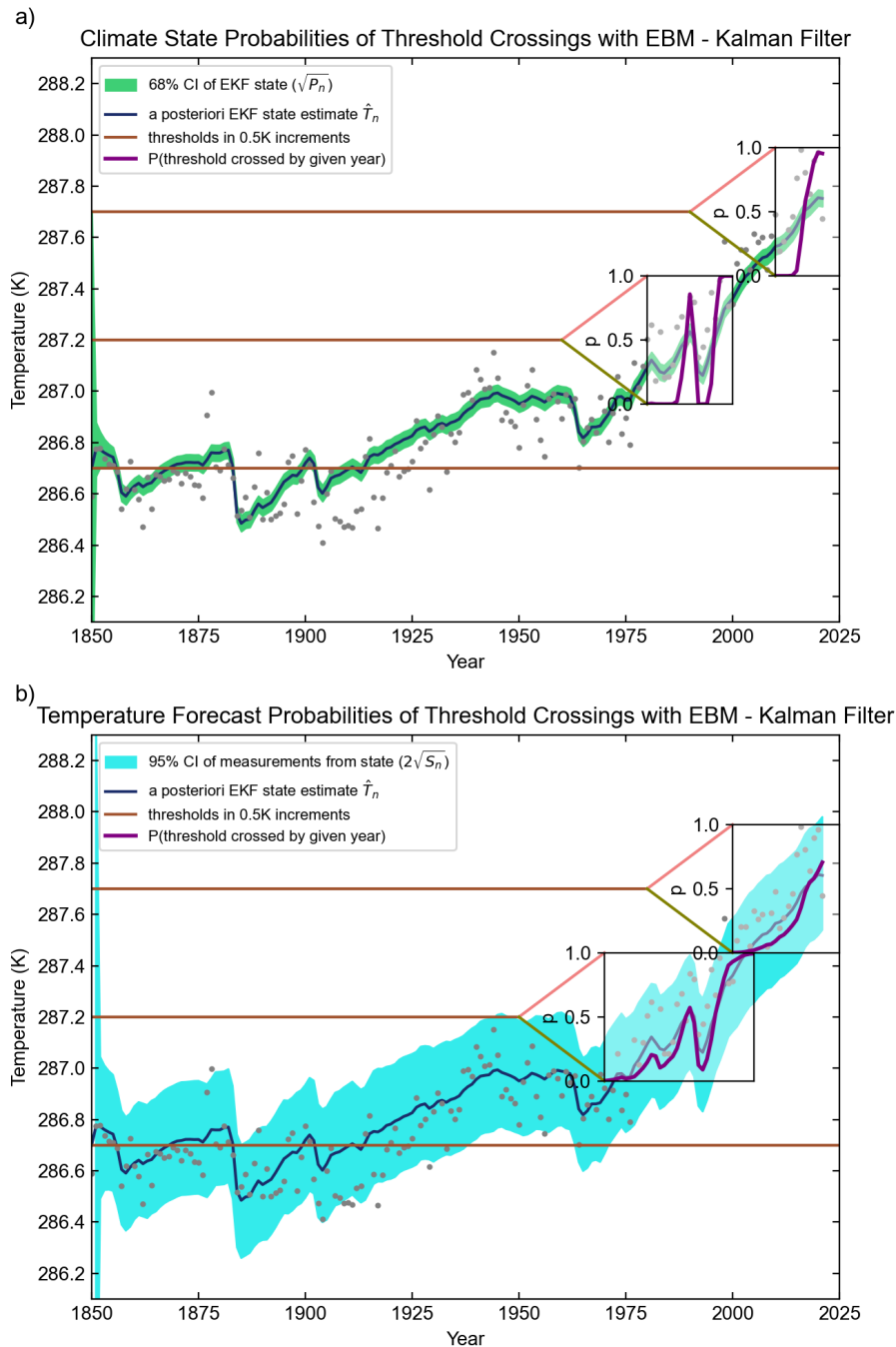
315 The IPCC AR6 (Lee, Marotzke et al.) states “the time of GSAT exceedance is
316 determined as the first year at which 21-year running averages of GSAT exceed the given
317 threshold”. This threshold exceedance by the climate state, as in the IPCC definition, is given
318 within the EBM-Kalman Filter by a Gaussian distribution (green in Fig. 4a) about the state \hat{T}_n

319 with a variance given by P_n . The IPCC has an ensemble of models to draw upon over both
320 the historical period and future projections, so the fraction of the 21-year means of each of
321 the ensemble members found above a given threshold determines the overall probability that
322 the climate threshold was crossed (assuming the ensemble spread is a good representation of
323 GMST uncertainty – recent IPCC reports instead widen the ensemble spread to approximate
324 the uncertainty range because coarse climate models under-represent internal variability and
325 model uncertainty: (Lee, Marotzke et al.), Box 4.1). The Kalman filter estimate does not
326 require this future projection, because it provides an instantaneous estimate of the "climate
327 state", and we can take simulated draws from this a posteriori state. In other words, the
328 probability of the "climate state" exceeding the threshold is the cumulative distribution
329 function (with mean μ set to the threshold and variance $\sigma^2=P_n$) at value of \hat{T}_n . Furthermore,
330 the EBM-Kalman Filter climate state covariance reflects the uncertainty in the 30-year
331 average of real-world GMST without empirical retuning.

332 Regarding the second meaningful interpretation of threshold crossing which we deem
333 "annual temperature forecast" above the threshold, the Kalman framework shows these
334 predictions as the window (blue in Fig. 4b) of possible next-year GMST measurements, a
335 Gaussian distribution centered at the projected state $\hat{T}_{n|n-1}$ with a variance given by the
336 innovation covariance (S_n): in other words, a simulated draw from the a priori state. This
337 uncertainty range reflects and encapsulates the actual real-world GMST measurements (see
338 Fig 3b). For an ensemble of climate models, the analogous "temperature forecast" probability
339 is the fraction of simulations at year x that are warmer than the threshold.

340 There is additional ambiguity regarding what "crossing a threshold" means regarding
341 any time-varying probability, especially given that due to volcanic eruptions these time-
342 varying probabilities may not monotonically increase (as is the case for a cumulative
343 distribution function). Here we define (based on the 1σ confidence interval, or the *likely*
344 range in IPCC terminology) the "threshold crossing period" to span from the earliest year
345 when $\geq 15.9\%$ of climate states or temperature forecasts exceed the threshold to the latest year
346 when $\leq 84.1\%$ of climate states or temperature forecasts exceed that threshold. We can further
347 note a "threshold crossing instant" to be the year(s) when the probability of exceeding the
348 threshold is nearest to 50% if successive years' probabilities cross 50% (or *as likely as not* to
349 have crossed the threshold in IPCC terminology). Regardless of whether a coupled climate
350 model or EBM-Kalman Filter is used, the temperature forecast method has a longer span of
351 threshold crossing period than the climate state because the uncertainty/ensemble spread in

352 the annual forecasts is wider than the uncertainty/ensemble spread of the time-averaged
 353 states, and both methods report similar threshold crossing instants (see Fig. 9).



354

355 Fig. 4: a) EBM-Kalman Filter and Climate State Thresholds: As in Fig. 3, there is the EBM-
 356 Kalman Filtered state estimate (navy blue line), a 1σ confidence interval of the model state
 357 covariance (P_n) in green blue, and GMST measurements in gray dots. Additionally, there are
 358 3 horizontal brown lines at 286.7K (the pre-industrial climate temperature), 287.2K (0.5K
 359 warmer than pre-industrial), and 287.7K (1.0K warmer than pre-industrial). The upper two

360 brown lines represent two climate thresholds which have already been passed, as indicated by
 361 the two inset boxes. Within these two inset boxes, the y-axis represents probability (from 0 to
 362 1) whereas the x-axis remains in years. The thick purple line within these inset boxes is the
 363 probability that the corresponding threshold was crossed by a given year. b) EBM-Kalman
 364 Filter and Temperature Forecast Thresholds: As in Fig. 3, there is the EBM-Kalman Filtered
 365 state estimate (navy blue line), a 2σ confidence interval of the innovation covariance (S_n) in
 366 light blue (around the a priori estimate). As in Fig. 4a, there are GMST measurements in gray
 367 dots, and 3 horizontal brown lines representing climate thresholds, the upper two at pre-
 368 industrial +0.5K and pre-industrial +1.0K. Within these two inset boxes, the y-axis represents
 369 probability (from 0 to 1) whereas the x-axis remains in years. The thick purple line within
 370 these inset boxes is the probability that the corresponding threshold was above a simulated
 371 draw from the a priori state.
 372

373 Note that both threshold crossing probabilities in thick purple track with the EBM-
 374 Kalman Filtered state estimate in thin blue in Fig. 4b when aligned by year, although these
 375 two quantities are in entirely different probability domains. This results from both state and
 376 innovation covariances that remain stable during this window, together with the fact that the
 377 cumulative density function of the Gaussian distribution is roughly linear in the vicinity of
 378 the mean. As the EBM-Kalman Filtered state estimate approaches any given threshold, the
 379 cumulative temperature threshold approaches 0.5, or 50% at a "threshold crossing instant".
 380 The +0.5K threshold had crossing instants in 1989, 1991, and 1996, while the +1.0K
 381 threshold's crossing instant was in 2017. For the temperature forecast, the threshold crossing
 382 periods were 1981-1998 for +0.5K, and 2013-present for +1.0K. As mentioned above, the
 383 threshold crossing periods for the climate state were briefer: 1988-1996 for +0.5K and 2016-
 384 2018 for +1.0K (see Fig. 9).
 385

386 4. Optional Refinements

387 a. Time-Varying Measurement Uncertainty and RT Smoother

388 This past-to-present Kalman Filter described in (5-13) can be extended into a RTS
 389 smoother (RTS) (Rauch, Tung et al. 1965) by additional steps (14-16), which encompass all
 390 known measurements into each estimated state by running backward from the last known
 391 estimates of \hat{x}_n and P_n .

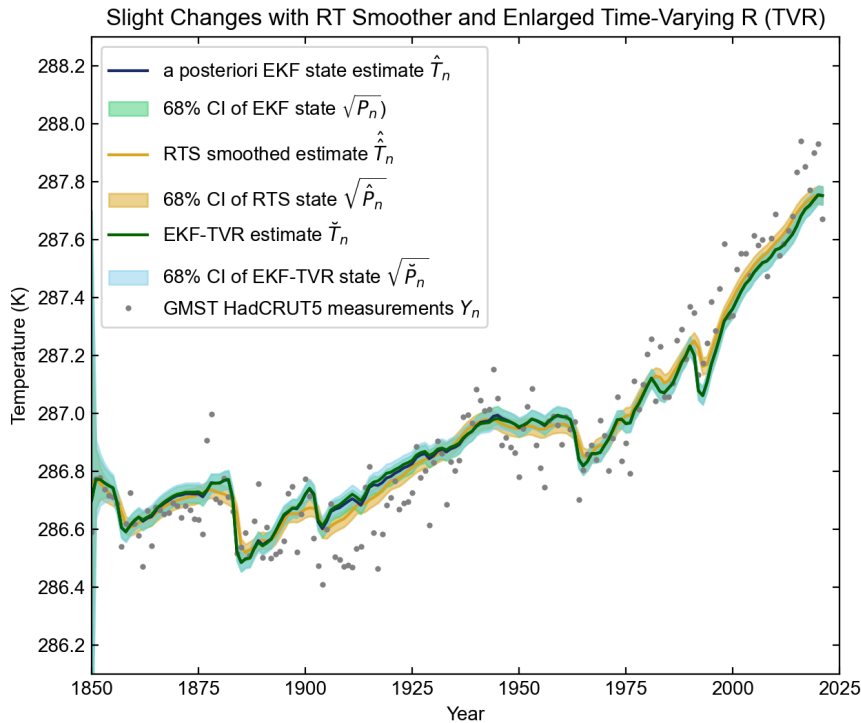
$$392 \quad \hat{K}_n = P_n \Phi_n / P_{n|n-1} \quad \text{back-updated Kalman gain} \quad (14)$$

$$393 \quad \hat{\hat{x}}_n = \hat{x}_n + \hat{K}_n \left(\hat{\hat{x}}_n - F(\hat{x}_n; u_{n+1}) \right) \quad \text{back-updated state estimate} \quad (15)$$

$$394 \quad \hat{P}_n = P_n + (\hat{P}_{n+1} - P_{n|n-1}) \hat{K}_n^2 \quad \text{back-updated state covariance} \quad (16)$$

395 This RTS has a theoretical advantage of blending abrupt changes in the model state over
396 greater time periods, while also slightly reducing the state covariance. For instance, if the
397 measurements suddenly and persistently diverged from the blind, forward EBM, an EBM-
398 Kalman Filter model state would only react as these measurements diverge, whereas an
399 EBM-RTS would foreshadow this jump. For the purposes of this paper, these distinctions
400 make little difference, as is demonstrated in Fig. 5 below. Note that between 1850 and 1860
401 the intentionally overestimated initial state uncertainty P_0 of 1K is reduced through
402 successive filtering steps in the EBM-Kalman Filter, and bi-directional smoothing steps
403 within the EBM-RTS.

404 The uncertainty in the climate state P_n automatically responds to unexpected values of
405 the measured temperature, which might occur if the weather variability in the climate
406 increases. (Wunsch 2020) Regardless of whether this dynamic occurs, measurement
407 uncertainty ought to reflect the improving global measurement system accuracy. Thus, an
408 alternative modification of the original EBM-Kalman Filter incorporates the known
409 uncertainty in the HadCRUT5 measurements of GMST, which decreases in standard
410 deviation from 0.079K in the 1850-1879 window to 0.017K in the 1990-2019 window (see
411 Figure 4 of HadCRUT5 (Morice, Kennedy et al. 2021)). This shrinking uncertainty primarily
412 reflects a lack of observations in the Southern hemisphere before the satellite age. The total
413 climate "emission" uncertainty can then be decomposed into two summed components: the
414 physical measurement uncertainty in GMST, and the state-to-measurement uncertainty
415 reflecting random-noise processes, sampling, and representativeness errors that make GMST
416 estimates deviate from the underlying climate state. We assume the covariance between these
417 two sources of uncertainty is 0 and simply sum the two variances to obtain a time-varying
418 value of R_n (TVR). In Fig. 5 this causes the EKF-TVR state uncertainty $\sqrt{\check{P}_n}$ to shrink from
419 its initial value of 1K slightly more slowly than $\sqrt{P_n}$, because for many decades there is
420 greater measurement uncertainty, so the filtering steps of this EKF-TVR cannot obtain as
421 much information from the early GMST measurements to constrain the uncertainty.



422
 423 Fig. 5: Comparisons of the original EBM-Kalman Filtered climate state (navy blue line with
 424 green 1σ uncertainty window) with an EBM-RTS climate state (red line with red 1σ
 425 uncertainty window) and the effects of incorporating additional time-varying measurement
 426 uncertainty (green line with light blue 1σ uncertainty window). The addition of extra time-
 427 varying measurement uncertainty makes very little difference to the EBM-Kalman Filtered
 428 climate state, except from 1905-1930 when it lessens the deflection of repeated cooler GMST
 429 temperature measurements. In contrast, the EBM-RTS climate state doubly takes these
 430 annual temperature measurements into account, so it has a greater cooling deflection in this
 431 period, and many years that are warmer than the EBM-Kalman Filtered climate state after
 432 1980, although even these differences are slight - at most 0.1K during years of volcanic
 433 activity.

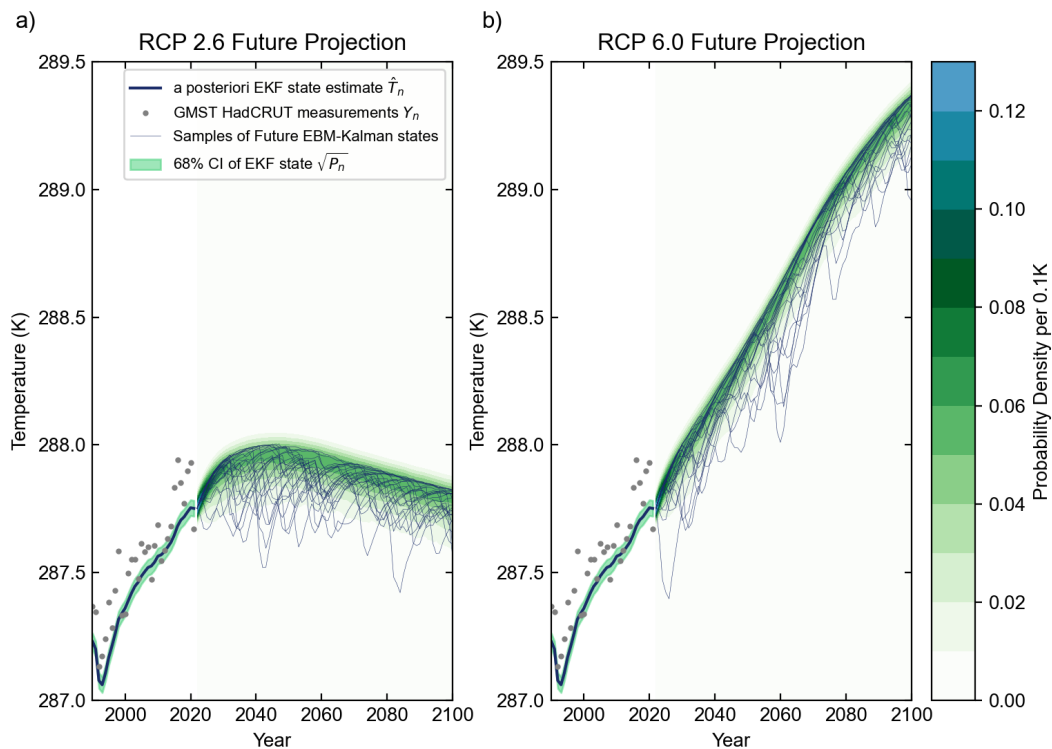
434

435 *b. Non-Gaussian Future Projection and Sampling of Volcanic Activity*

436 Any EBM-Kalman Filter can project into the future without any new measurements.
 437 This simply involves repetitively using just equations 2.2 and 2.3, and then taking the a
 438 posteriori state and a posteriori covariance to be the a priori (projected) state and a priori
 439 covariance: $\hat{\mathbf{x}}_n = \mathbf{F}(\hat{\mathbf{x}}_{n-1})$ and $\mathbf{P}_n = \Phi_n^2 \mathbf{P}_{n-1} + \mathbf{Q}$. While this means that the state covariance is
 440 linearly growing, here \mathbf{Q} is very small (variance ~ 0.00037), and so over a 79-year future
 441 projection (2022-2100) the state covariance only grows from a 1σ uncertainty of 0.0307K to
 442 between 0.0352K and 0.0355K, a 16% increase that is imperceptible over this century (Fig.
 443 6).

444 A slightly more complex issue regarding future projections is generating the two time
 445 series inputs into the blind EBM, namely the concentrations of greenhouse gasses including
 446 carbon dioxide ($[CO_2]_n$) and stratospheric aerosols due to volcanic dust (AOD_n). Future
 447 carbon dioxide concentrations are given by representative concentration pathways (RCPs),
 448 which numbered according to the projected CO_2 radiative forcing in 2100 relative to the
 449 preindustrial climate (<https://tntcat.iiasa.ac.at/RcpDb/>). For instance, we picked RCP2.5 and
 450 RCP6.0 in Fig. 6, which flank the most likely result of current environmental policies. (Pielke
 451 Jr, Burgess et al. 2022). Volcanic eruptions determining AOD_n are inherently stochastic, but
 452 the time intervals between eruptions can be approximated using exponential distributions
 453 (Papale 2018). No single exponential distribution fits well to the observed series of time
 454 intervals, so an exponential mixture with two components was found to be the best fit to the
 455 data using the decomposed normalized maximum likelihood. (Okada, Yamanishi et al. 2020)
 456 See Appendix C for further details.

457 While these distribution approximations may be imperfect from the perspective of a
 458 volcanologist, for our purposes they simply allow reasonable-looking samples of future
 459 aerosol optical depths to be fed into the EBM-Kalman Filter. Even though the EBM-Kalman
 460 Filter is built on the assumption of Gaussian error, it is so computationally simple that it can
 461 be used to sample complex non-Gaussian distributions.



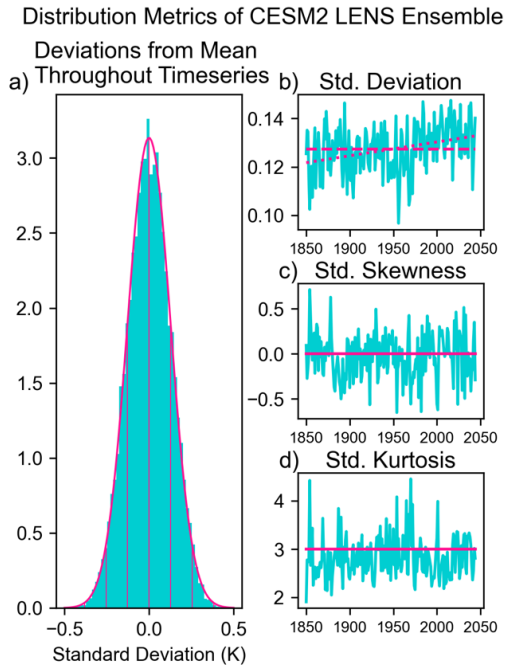
462

463 Fig. 6: Future projections of RCP2.6 (6a) and RCP6.0 (6b) scenarios using sampled measures
464 of volcanic activity. RCP2.6 in Fig 6A is a very stringent future scenario in which CO₂
465 emissions sharply decline after 2020 to keep GMST rise below 2°C (van Vuuren, den Elzen
466 et al. 2007). RCP6.0 in Fig 6B is a much higher emission scenario in which CO₂ emissions
467 do not peak until 2080 (Fujino, Nair et al. 2006; Hijioka, Matsuoka et al. 2008). The median
468 estimate based on current environmental policies projects warming of 2.2°C to reach a
469 GMST of 288.9K by 2100. (Pielke Jr, Burgess et al. 2022). The historical Mt. Pinatubo
470 eruption in 1991 is shown in the lower left corner of both graphs for scale. 25 of the sampled
471 500 potential future climate states are graphed as thin navy-blue lines. The probability density
472 function formed by taking the summation of all sampled gaussian kernels at each time point
473 is shaded in green. Note that this probability density is not symmetrical - there is a much
474 more gradual tapering off on the cooler side because of volcanic eruptions. Indeed, the
475 volcanic eruptions dominate the future uncertainty over the slowly growing state uncertainty.
476 There is a gap from 2021 to 2022 between the past EKF state estimates and future
477 projections, to emphasize the distinction between these even though the same state estimate
478 and state covariance is carried forward in time for each future sample.
479

480 **5. Discussion**

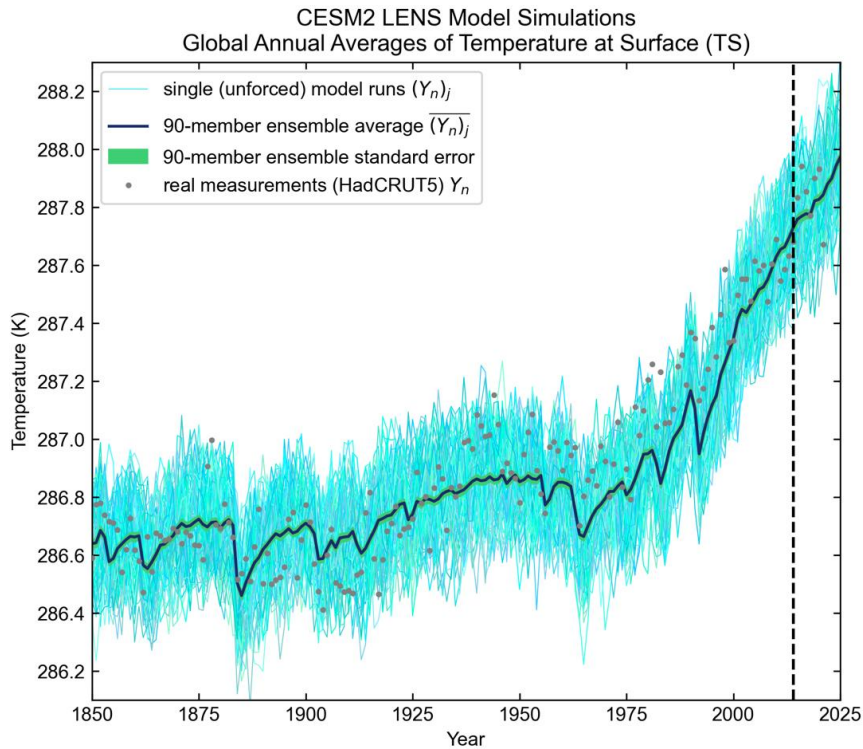
481 *a. Comparison to a Large Coupled Model - CESM2*

482 The EBM-Kalman Filter framework is chiefly advantageous because it replicates the major
483 statistical features of an ensemble of large coupled climate models, while being trivial to
484 compute. Therefore, we analyze the statistical features of one such ensemble, particularly the
485 [90 runs](#) of LENS2 (Rodgers, Lee et al. 2021). The distribution of annual differences of all
486 model trajectories from the ensemble mean are remarkably close to Gaussian. (Fig. 7)
487 Therefore, this fundamental assumption of the EBM-Kalman Filter is also met by the CESM2
488 large coupled climate model. While the standard deviation does rise with time in this large
489 ensemble ($p=0.002$) indicating increasing internal variability with climate change, this effect
490 was relatively small ($r^2=0.105$ and the rise was only 9.4% from 1850-2050). The time-
491 averaged standard deviation of 0.127K was close to both the chosen value of $\sqrt{(R)} = 0.105K$
492 and to the converged value in the EBM-Kalman Filter of the innovation covariance $\sqrt{S_n} =$
493 0.110K.



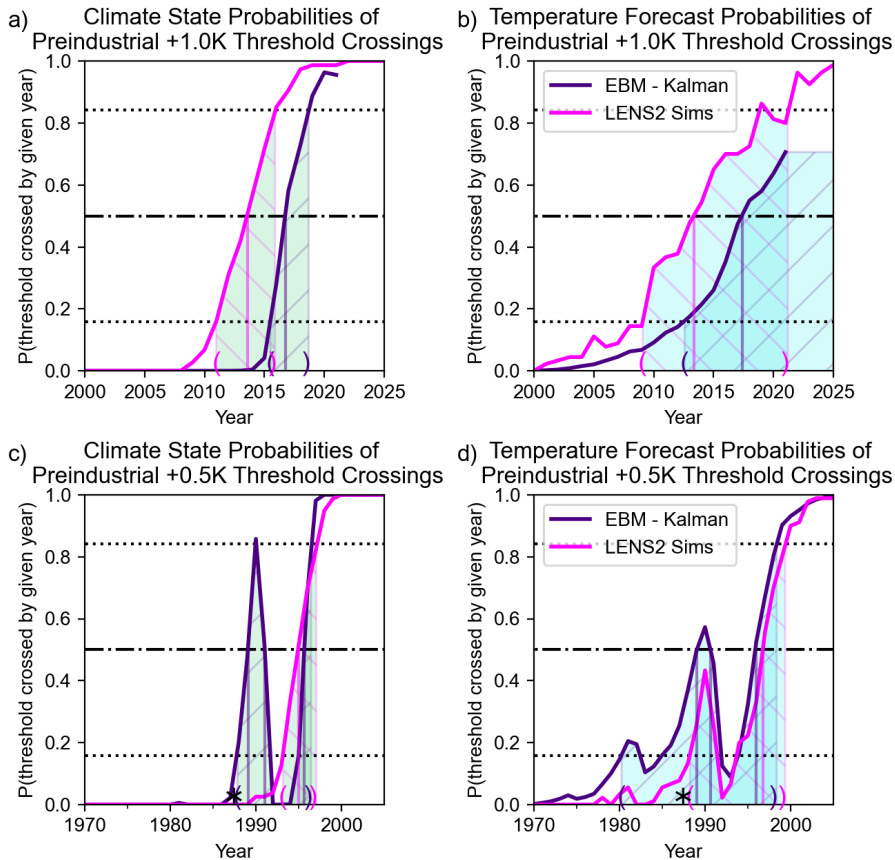
494
 495 Fig. 7: Statistical Features of the CESM2 Large Ensemble. (Rodgers, Lee et al. 2021). Pink
 496 lines in the histogram in (7a) depict an ideal Gaussian distribution with standard deviation of
 497 0.126K, and vertical lines drawn for each of these standard deviations. Solid pink lines for the
 498 skewness and kurtosis indicate the ideal values for a Gaussian distribution. The observed
 499 trend in the standard deviation over time is plotted in a dotted pink line in the top-right
 500 corner.

501
 502 Next, we evaluated how well this LENS2 captures the overall shape of the observed
 503 HadCRUT5 temperatures, given that it is not constrained directly by these observations. We
 504 wish to draw attention to the fact that in order to create this figure, the absolute temperature
 505 of the LENS2 runs had to be revised down by a full 1.75K to match the 1960-1990 30-year
 506 climate normal (Jones and Harpham 2013). Other authors have also noted this high absolute
 507 temperature as well as the high climate sensitivity of CESM2. (Gettelman, Hannay et al.
 508 2019; Feng, Otto-Bliesner et al. 2020; Zhu, Otto-Bliesner et al. 2022)



509
 510 Fig. 8: Comparison of the CESM2 Large Ensemble (LENS2). (Rodgers, Lee et al. 2021) with
 511 HadCRUT5 measurements. The various shades of thin light blue and turquoise lines
 512 represent each individual simulation $(Y_n)_j$ of the 90-member ensemble. The ensemble mean is
 513 plotted in a navy-blue line, and the ensemble standard error is plotted around this line in
 514 green. This standard error in green is the standard deviation divided by the square root of the
 515 number of runs in the ensemble at that moment and shows the 1σ uncertainty in the yearly
 516 simulated climate is roughly 0.013K. Also, the ensemble mean has $r^2 = 0.83$ relative to the
 517 HadCRUT5 measurements, slightly lower than for the blind EBM. The dashed vertical line
 518 represents future simulations at the time of the construction of LENS2.

519
 520 Regarding the various types of climate thresholds, the LENS2 can be used to generate very
 521 similar results to the EBM-Kalman Filter. Differences in absolute probability and threshold
 522 crossing instants reflect differences in the modeled climate states: particularly that the
 523 CESM2 was cooler than the energy-balance model in the 1980s and 1990s, whereas the
 524 opposite was the case after 2000 (Fig. 9).



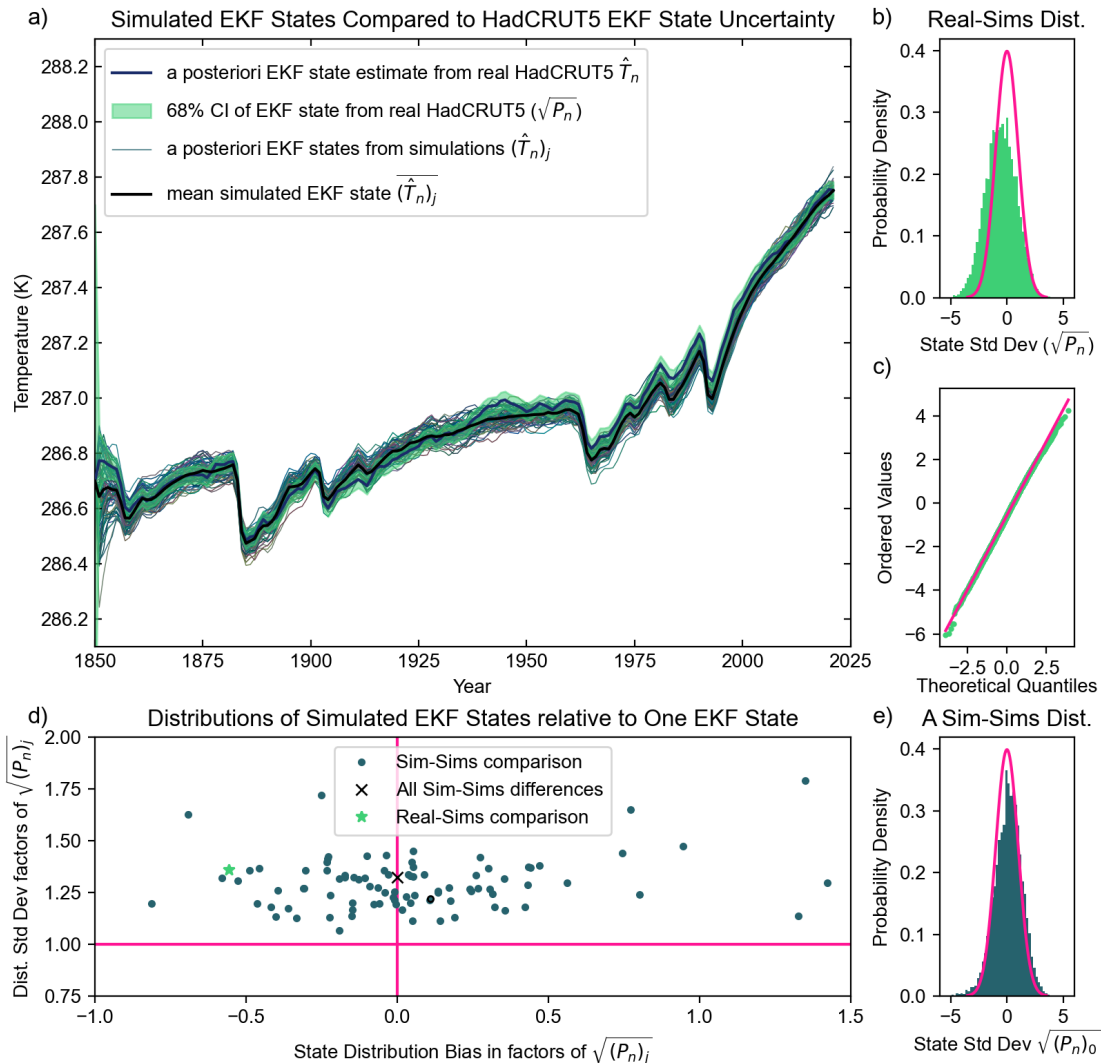
525
 526 Fig. 9: Comparison of Historical Threshold Crossing Probabilities for the EBM-Kalman
 527 Filter (dark purple) and CESM2 LENS simulations (pink). Note that the dark purple lines are
 528 the same as those graphed in the inset axes within Figure 4. The left panels (a and c) display
 529 probabilities relevant to climate states with 21-year averages of the CESM2 simulations,
 530 whereas the right panels (b and d) display the temperature forecasts. Top panels (a and b)
 531 display the preindustrial +1.0K threshold, whereas the bottom panels (c and d) display the
 532 earlier preindustrial +0.5K threshold. Additionally, the threshold crossing instants are marked
 533 with thick vertical lines within all panels. The threshold crossing windows are lightly shaded
 534 and hashed: with light blue shading for temperature forecast windows, light green shading for
 535 climate state windows, positively sloping hashing in dark purple for the EBM-Kalman Filter,
 536 and negatively sloping hashing in pink for LENS2. The cross-hatched regions indicate where
 537 the EBM-Kalman Filter and LENS2 agree regarding the threshold crossing windows. The
 538 limits of these crossing windows are also drawn with parentheses on the time axis in dark
 539 purple for the EMB-Kalman filter and pink for LENS2. A black asterisk indicates 1987, the
 540 year that 30-year running mean of GMST crossed the +0.5K threshold in the bottom panels (c
 541 and d), whereas the latest 30-year mean centered in 2007 is below the +1.0K threshold.
 542

543 We also compared future EBM-Kalman Filter projections with LENS2 projections. Both
 544 graphs trace out roughly the same shapes, although the SSP370 experiment portion of the
 545 LENS follows RCP7.0, which had more intense forcing than what was projected in RCP6.0
 546 (see Figure 6B). Also, the largely symmetric variation in the large coupled model is driven by
 547 dynamical instability. This is fundamentally different from the EBM-Kalman Filter, which

548 samples a noisy distribution of volcanic eruptions, yielding asymmetrical variation. This
549 illustrates a major advantage of this system: thousands of future scenario inputs can be
550 generated and utilized within seconds on a mere personal computer (see Fig. 6). In contrast,
551 each of the LENS2 simulations took over a week to run on part of a supercomputer cluster
552 ($>10^{10.5}$ times slower) and gave every simulation an identical projection of volcanic activity:
553 an aerosol optical depth prescribed to a fixed annual cycle depending on latitude and altitude.

554 *b. Sampling from a member - need to enlarge the model uncertainty for ensemble spread*

555 There are many more past and future climate scenarios that researchers wish to
556 investigate than there are computational resources to run a full large coupled ensemble for
557 each scenario. Fortunately, the EBM-Kalman Filter allows for one or a handful of large
558 coupled climate model simulations to approximate the distribution of an entire ensemble
559 spread (similar to an approach taken for ensembles of ice sheet models in (Edwards, Nowicki
560 et al. 2021)). The average “climate state uncertainty” $\sqrt{P_n}$ following one model ensemble
561 member ($\sim 0.038\text{K}$) nearly covers the spread of “climate states” $(\hat{T}_n)_j$ within the entire LENS2
562 simulation ensemble (Fig 10a,e), which relative to each other are distributed with a standard
563 deviation that is only 1.32 times larger. So the EBM-Kalman Filter approximates what “state
564 uncertainty” intuitively means within the context of a large coupled ensemble, a result
565 especially remarkable because the error terms (R and Q) were based on the HadCRUT5
566 dataset alone, not LENS2. HadCRUT5 measurements themselves can also roughly
567 approximate the LENS2 “state uncertainty” (see Fig. 10a,b,c). However, there are inter-
568 annual differences which persist between runs of the ensemble and skew some climate states
569 $(\hat{T}_n)_j$ cooler and others warmer (Fig. 10d). Also, it is unknown if the current generation of
570 large coupled climate models have the ability to represent the full spread of climate states
571 appropriately. For instance, weather models use stochastic variation to push their distribution
572 wider than dynamic variation alone (Buizza, Milleer et al. 1999), and the IPCC interprets the
573 2-sigma ensemble spread as the probability range associated with only a 1-sigma spread
574 ((Lee, Marotzke et al. 2021), Box 4.1). Therefore, we empirically recommend doubling $\sqrt{P_n}$
575 to cover a distribution of unknown “climate states” based on a single simulation.



576
 577 Fig. 10: Comparison of the Kalman Filter States across the LENS2 ensemble. a) The mean
 578 Kalman Filtered state estimate (thick black line) is drawn with all individual Kalman Filtered
 579 state estimates assimilating individual CESM2 simulations (rather than measurements of real
 580 GMST) also drawn as blue-gray lines. A 1σ state confidence interval is shown around the
 581 HadCRUT5 measured GMST's Kalman Filtered climate state (light green area). b) The
 582 differences between the "real" measurement based HadCRUT5 climate state and all LENS2
 583 climate states, scaled by the state standard deviation and plotted against the ideal normal
 584 distribution. The empirical and ideal distributions approximately match, demonstrating that
 585 even without adjustment the majority of LENS2 climate states are within the climate state
 586 uncertainty window assumed by the original HadCRUT5-based EBM-Kalman Filter. c) In the
 587 qqnorm plot, these differences between the "real" measurement based HadCRUT5 climate
 588 state and all LENS2 climate states nearly follow a straight line. d) Climate states and
 589 associated uncertainties arising from each of 89 LENS2 simulations and HadCRUT5 are
 590 compared to all other LENS2 climate states, and the bias and standard deviation of the
 591 resulting empirical distributions are plotted. One LENS2 simulation had early missing data,
 592 preventing the EBM-Kalman from running on it. e) One of these empirical distributions is
 593 graphed, indicated by the point circled in black within the scatterplot.
 594

595 *c. Future Extensions*

596 We emphasize that this first iteration of a climate Kalman filter does not generate
597 regional temperatures nor other essential climate variables, such as precipitation. It also does
598 not capture regional “tipping points” or other important nonlinear process aspects of climate
599 change. Therefore, this first climate Kalman filter is far from generating the information
600 required to compare it to large ensembles. However, we also note that this Kalman
601 framework was designed to be utilized on a vector of state parameters, and we are only
602 currently utilizing scalar values of GMST. Other terms in a potential global climate state
603 vector, such as precipitation, seasonal temperature, or eigenvalues of spatially decomposed
604 principal components of the climate system (for instance the El Nino / Southern Oscillation)
605 could be appended into this Kalman framework with appropriate simple physical forward
606 modeling. (Yang, Li et al. 2018)

607 Additionally, we experimented with Bayesian parameter search to give better
608 estimates of the coefficients in the blind energy-balance equation. The prior distributions of
609 these coefficients can be extracted from climate science literature, followed by a Metropolis-
610 Hastings search. However, identifiability and overfitting remain challenging and deserve
611 more attention than the scope of this introduction allows. Several parameters must be tuned
612 proportionally for certain constraints to be maintained (particularly no net energy transfer in
613 the preindustrial climate), such as the main coefficient multiplying all longwave radiation
614 terms and the power on the temperature (currently 2.385 in the original energy-balance
615 model). Astute readers may observe that the most recent years of the blind energy-balance
616 model (and thus the Kalman filtered state) appear cooler than both the Hadcrut5 and the
617 CESM2 LENS predictions. We decided to use all point estimates given by literature sources
618 rather than tuning any feedback to avoid unnecessary complexity. But this issue of
619 underestimating the recent climate may be most directly fixed by increasing the CO₂
620 feedback to a greater W/m² of energy absorbed per order of magnitude of CO₂ increase (see
621 Eq. A15). This change would represent a larger forcing due to anthropogenic atmosphere
622 changes that scale with CO₂, or reduced reflective aerosol feedbacks to offset these forcings
623 (see Fig 7.6 of Forster et al. 2021).

624 Finally, the Kalman filtering framework may be utilized in process control (Myers
625 and Luecke 1991; Lee and Ricker 1994) to optimize various climate change mitigation
626 strategies (Filar, Gaertner et al. 1996; MacMartin, Kravitz et al. 2014; Kravitz, MacMartin et
627 al. 2016).

628

629 **6. Conclusion**

630 The EBM-Kalman Filter presented in this paper represents somewhat of a
631 compromise between a 30-year running average of GMST (the historical definition of
632 climate) and the state-of-the-art large coupled climate model ensembles such as CESM2
633 LENS. The variance of the EBM-Kalman Filtered climate state is easily constructed to be
634 very close to that of a running 30-year mean, and this filtered climate state then does an
635 excellent job in describing the overall shape of the measured temperature values (as indicated
636 by a R^2 of 0.88). However, this EBM-Kalman Filter has no lag: as soon as measured values
637 are reported for the current year, it can describe the climate state, unlike the 30-year mean
638 which can only describe what the climate was 15 years ago. In comparison to the ensemble
639 spread of an ensemble of coupled climate models, which is presently the typical brute-force
640 method for quantifying internal variability, there is a very similar Gaussian statistical
641 distribution. In contrast the EBM-Kalman Filter approach has very transparent, clean physical
642 parameters that can be directly measured (or taken from estimates in literature) leading to
643 trivial uncertainty quantification. The computational cost of the EBM-Kalman Filter is
644 negligible, so future predictions can sample from probability distributions which approximate
645 intermittent volcanism, unlike coupled climate models. This EBM-Kalman Filter framework
646 can additionally be used to easily calculate various definitions of climate thresholds, which
647 have significant implications for policy. While it does not predict all climate variables of
648 interest, it is a powerful, transparent, and inexpensive tool that may be readily combined with
649 other approaches.

650 *Acknowledgments.*

651 JMN, BFK, and CL were funded by ONR N00014-17-1-2393. Conversations with
652 Jochem Marotzke and Lorraine E. Lisiecki helped to focus this work.

653 *Data Availability Statement.*

654 Data analyzed in this study were a re-analysis of existing data, which are openly available
655 at locations cited in the main text, appendices, and reference section. Further documentation
656 about data processing including Python code is available at the Brown Digital Repository at
657 [*insert DOI here*].

Appendix A: Derivation of the Blind Energy-Balance Model

660 Units are omitted in this section within equations for clarity of the mathematical derivation,
661 but they are retained within the text and reincorporated in A32 and A24.

$$662 \quad \Delta \text{Energy} = \phi_{\text{SW}}(\text{in}) - \phi_{\text{LW}}(\text{out}) \quad (\text{A1})$$

$$663 \quad \frac{T_{n+1} - T_n}{k} C_{\text{heat}} = G_0 * \tilde{d}_n * f_{\alpha A}(T_n) * f_{\alpha S}(T_n) - j^* * \tilde{g}_n * f_{H_2O}(T_n) \quad (\text{A2})$$

664 k is 1 year, the time step of this iterative model. n represents the calendar year (e.g. 2000). On
665 the right side of the equation, both the shortwave radiative flux and longwave radiative flux
666 take the same form: (source) * (prescribed attenuation) * (feedback attenuation). C_{heat} , the
667 heat capacity of the climate system, was known imprecisely: $17 \pm 7 \text{ W (year) m}^{-2} \text{ K}^{-1}$,
668 (Schwartz 2007), however this heat capacity value has a relatively minor impact on the
669 overall model performance.

670 G_0 is the extraterrestrial irradiance, taken to be (solar irradiance)/4 = $1360 \text{ W/m}^2 / 4 = 340$
671 W/m^2 . While the annual extraterrestrial irradiance varies by 0.1% between solar minima and
672 solar maxima on a cycle lasting about 11 years (Willson and Hudson 1991; Wang, Lean et al.
673 2005; Kopp and Lean 2011), within this model it was assumed a constant.

674 \tilde{d}_n is the prescribed shortwave light attenuation due to volcanic dust. This stochastically
675 varying quantity can be calculated from the stratospheric optical depth AOD_n (Sato, Hansen
676 et al. 1993; Vernier, Thomason et al. 2011) according to the formula given by Harshvardan
677 and King (1993; Schwartz, Harshvardhan et al. 2002). ($g=0.853$ is the middle of the given
678 range). The AOD_n values used are used as forcings for the [GISS climate model](#) from 1850 -
679 1978 (AOD_n at 550nm) and globally averaged measurements from the [GloSSAC_V2](#) satellite
680 measurement product (Nasa/Larc/Sd/Asdc 2018) from 1979 – 2021 (AOD_n at 525nm).

$$681 \quad \tilde{d}_n = \frac{1.33}{\text{AOD}_n * (1-g) + 1.43}, \quad g \in [0.834, 0.872] \quad (\text{A3})$$

$$682 \quad \tilde{d}_n \approx \frac{9.07}{\text{AOD}_n + 9.73} \quad (\text{A4})$$

683 $f_{\alpha A}(T_n)$ is the additional atmospheric shortwave attenuation due to cloud albedo, while $f_{\alpha S}(T_n)$
684 is the surface shortwave attenuation due to ground albedo. Taken together, these two terms
685 yield an overall absorption of 0.707 as measured by the measured from March 2000 to
686 February 2005 by the CERES satellite (Wielicki, Barkstrom et al. 1996; Loeb, Wielicki et al.

687 2009), or equivalently a top-of-atmosphere, all-sky albedo of 0.293. Decomposition of this
 688 overall albedo into its clear-sky component (0.153) yields a ground absorption fraction of
 689 0.847. Noting the small volcanic dust in the atmosphere during this time frame, the total
 690 shortwave attenuation can be used to solve for both components:

$$691 \quad 0.707 \approx \tilde{d}_n * f_{\alpha A}(T_n) * f_{\alpha S}(T_n) \approx \frac{9.07}{0.002+9.73} * f_{\alpha A}(T_n) * 0.847 \quad (A5)$$

$$692 \quad 0.896 \approx f_{\alpha A}(T_n), \quad \text{for } n \in [2000, 2005] \quad (A6)$$

693 $j^* = \sigma_{sf} T_n^4$ is the ideal black body radiation or Planck feedback, which derives from quantum
 694 mechanics, particularly the Stefan-Boltzmann law (Boltzmann 1884), which gives the Stefan-
 695 Boltzmann constant $\sigma_{sf} = 5.670 \cdot 10^{-8} \text{Wm}^2\text{K}^{-4}$ as a coefficient. For the Earth, because the
 696 temperature is in the neighborhood of 287K, this black body radiation is primarily in the
 697 infrared spectrum, between 200 and 1200 cm^{-1} (Zhong and Haigh 2013).

698 \tilde{g}_n is the prescribed longwave attenuation due to CO_2 , which is half of the fraction of radiative
 699 energy absorbed by those CO_2 (because half is re-emitted upwards and half downwards). This
 700 absorbed, downwards-emitted fraction is directly proportional by β_0 to the logarithm of the
 701 CO_2 concentration (see Figure 6b of (Zhong and Haigh 2013)). CO_2 concentrations were
 702 taken as the historical concentrations used in the NASA GISS climate model 1850-1979
 703 (<https://data.giss.nasa.gov/modelforce/ghgases/Fig1A.ext.txt>) and the NOAA global averages
 704 from 1980-2021 (https://gml.noaa.gov/webdata/ccgg/trends/co2/co2_annmean_gl.txt).

$$705 \quad \tilde{g}_n = \frac{E_{\text{absorbed}}}{2j^*} \approx \beta_0 + \beta_l \log_{10}([\text{CO}_2]_n) \quad (A7)$$

706 $f_{\text{H}_2\text{O}}(T_n)$ is the additional atmospheric longwave attenuation due to water vapor and other
 707 gasses, including both lapse rate and relative humidity. The precise functional form of this
 708 feedback function is unknown, as is the functional form of the two shortwave feedbacks,
 709 partially due to disagreements between paleoclimate inferences and globally coupled climate
 710 models. We thus introduced the following 3 functions, which incorporate an additional 3
 711 positive β coefficients and 1 exponent. (Note $p_0=4$, the exponent on the j^* term.)

$$712 \quad f_{\text{H}_2\text{O}}(T_n) \doteq (1/T_n)^{p_1} \quad (A8)$$

$$713 \quad f_{\alpha A}(T_n) \doteq 0.896(1 + \beta_2(T_n - T_{2002})^{p_2}) \quad (A9)$$

$$714 \quad f_{\alpha S}(T_n) \doteq 0.847(1 + \beta_3(T_n - T_{2002})^{p_3}) \quad (A10)$$

715 Now, following the definition of climate sensitivity of z as $\partial N/\partial w * dw/dT$, where N
716 is the TOA radiative flux (the entire right side of the model), we expressed the climate
717 sensitivity of each of the three f feedback functions and the Planck response j^* , as reported in
718 Table 7.10 and Figure 7.10 of AR6 (Forster, Storelvmo et al. 2021).

$$719 \quad \frac{\partial N}{\partial j^*} * \frac{dj^*}{dT_n} = -\tilde{g}_n * f_{H2O}(T_n) * 4\sigma_{sf}(T_n)^3 = -3.22 \quad (A11)$$

$$720 \quad \frac{\partial N}{\partial f_{H2O}(T_n)} * \frac{df_{H2O}(T_n)}{dT_n} = -j^* * \tilde{g}_n * -p_1(T_n)^{-p_1-1} = 1.30 \quad (A12)$$

$$721 \quad \frac{\partial N}{\partial f_{aA}(T_n)} * \frac{df_{aA}(T_n)}{dT_n} = 340 * \tilde{d}_n * f_{aS}(T_n) * 0.896\beta_2 = 0.35 \quad (A13)$$

$$722 \quad \frac{\partial N}{\partial f_{aS}(T_n)} * \frac{df_{aS}(T_n)}{dT_n} = 340 * \tilde{d}_n * f_{aA}(T_n) * 0.847\beta_3 \approx 0.42 \quad (A14)$$

723 Solving for the exponent by taking the ratio of the first two equations yielded $p_1=1.615$.
724 Furthermore, based on the CERES measurements from 2000-2005, everything to the left of
725 both β_2 (A13) and β_3 (A14) is the overall absorbed SW radiance of $340*0.707=240.5$ W/m²,
726 so $\beta_2 = 0.00146$ K⁻¹ and $\beta_3 = 0.00175$ K⁻¹.

727 Figure 3.3 from Zhong and Haigh (2013) shows that per order of magnitude of [CO₂]
728 increase, an additional 15.45 W/m² is absorbed. Because there are additional anthropogenic
729 greenhouse gasses such as methane, the net contribution is slightly higher than this, by a
730 fraction of 2.72 W/m² / 2.16 W/m², so assuming CO₂ remains the same proportion to these
731 other gasses, an additional 19.45 W/m² is absorbed per unit of log₁₀ [CO₂] increase. (see AR6
732 (Forster, Storelvmo et al. 2021), Figure 7.6 and Table 7.8) This measurement approximating
733 a partial derivative was presumably made recently, so we used the more recent 2002
734 temperature of ~ 287.5 K (14.4°C), but this choice is relatively inconsequential: $\beta_0\beta_1$ would be
735 only 0.66% larger if the pre-industrial temperature were used instead. In the pre-industrial
736 climate, we assumed a steady-state equilibrium with a constant black body temperature of
737 286.7K (13.6°C) and a log₁₀([CO₂]) ≈ 2.45 . This allows us to solve for β_0 and β_1 as follows:

$$738 \quad 19.45 = \frac{\partial N}{\partial f_{H2O}(T_n)} * \frac{df_{H2O}(T_n)}{d \log_{10}([CO_2]_n)} = -\sigma_{sf}(T_n)^4 \beta_I(T_n)^{-1.61} (-\beta_0) \quad (A15)$$

$$739 \quad 456.4 = \beta_I \beta_0 \quad \text{using } T_{2002} = 287.5 \quad (A16)$$

$$740 \quad 0 = 340 \tilde{d}_n * f_{aA}(T_{1850}) * f_{aS}(T_{1850}) - \sigma_{sf}(T_{1850})^4 \beta_I(T_{1850})^{-1.61} (1 - \beta_0(2.45)) \quad (A17)$$

$$741 \quad 241.1 = \sigma_{sf}(286.7)^{2.39} (\beta_I) (1 - \beta_0(2.45)) \quad (A18)$$

$$742 \quad 5656 = (\beta_I) (1 - \beta_0(2.45)) \quad (A19)$$

743

$$744 \quad 6972 \approx \beta_1 \quad \text{and} \quad 0.0655 \approx \beta_0 \quad (\text{A20})$$

745 Checking that Planck partial derivative is accurate, we obtained a value for climate sensitivity
 746 of j^* to be $-3.34 \text{ W/m}^2/\text{K}$ at current conditions and the sensitivity of f_{H2O} to be $1.35 \text{ W/m}^2/\text{K}$,
 747 well within the likely range of AR6. However, with an instantaneous doubling or quadrupling
 748 of CO_2 the sensitivity of j^* becomes $-3.30 \text{ W/m}^2/\text{K}$ or $-3.22 \text{ W/m}^2/\text{K}$ respectively. Because
 749 they were defined to have proportional climate sensitivities, f_{H2O} exactly matches AR6 in a
 750 $4\times\text{CO}_2$ scenario, with $1.30 \text{ W/m}^2/\text{K}$.

751 This yielded a blind energy-balance model with good skill at predicting the GMST
 752 (orange dashed line in Fig. 2), $r^2 = 0.88$. Reducing and differentiating:

$$753 \quad T_{n+1} = T_n + 137.65 \frac{(1+0.00146(T_n-287.5))(1+0.00175(T_n-287.5))}{\text{AOD}_n+9.73}$$

$$754 \quad -0.00002325(T_n)^{2.39} (1-0.0655 \log_{10}([\text{CO}_2]_n)) \quad (\text{A21})$$

$$755 \quad \frac{\partial T_{n+1}}{\partial T_n} = 1 + \frac{0.441}{\text{AOD}_n+9.73} (1+0.00159(T_n-287.5))$$

$$756 \quad -0.00005546(T_n)^{1.39} (1-0.0655 \log_{10}([\text{CO}_2]_n)) \quad (\text{A22})$$

757 Further simplifying to nondimensionalize all units:

$$758 \quad T_{n+1} = T_n + \frac{137.7\text{m}}{\text{AOD}_n+9.73\text{m}} \left(1 + \frac{T_n-287.5\text{K}}{687.1\text{K}}\right) \left(1 + \frac{T_n-287.5\text{K}}{572.6\text{K}}\right)$$

$$759 \quad - \left(\frac{T_n}{274.9\text{K}}\right)^{2.385} \log_{10} \left(\frac{1.893 \cdot 10^{15} \text{ppm}}{[\text{CO}_2]_n}\right) = F(T_n; [\text{CO}_2]_n, \text{AOD}_n) \quad (\text{A23})$$

$$760 \quad \frac{\partial T_{n+1}}{\partial T_n} = 1 + \frac{0.4407\text{m}}{\text{AOD}_n+9.73\text{m}} \left(1 + \frac{T_n-287.5\text{K}}{629.9\text{K}}\right)$$

$$761 \quad - \left(\frac{T_n}{8464\text{K}}\right)^{1.385} \log_{10} \left(\frac{1.893 \cdot 10^{15} \text{ppm}}{[\text{CO}_2]_n}\right) = \frac{\partial F(T_n; [\text{CO}_2]_n, \text{AOD}_n)}{\partial T_n} \quad (\text{A24})$$

762

763 **Appendix B: Justification that the EKF is sufficient, will not diverge**

764 The issue of nonlinearity arises not in the computation of $\hat{x}_{n|n-1} = F(\hat{x}_{n-1})$ but rather the
 765 covariance distribution P_n of points (infinitesimal probability masses) neighboring \hat{x}_{n-1} , which
 766 are assumed to scale linearly around this transformation to maintain a normal distribution.
 767 Nonlinear distortion may pile more probability density onto a state other than the transformed
 768 original projection $F(\hat{x}_{n-1})$, necessitating a new computation of $\hat{x}_{n|n-1}$ as the mean of this

769 distorted PDF. Thus, for an arbitrary point that is z standard deviations away from \hat{x}_{n-1} , the
 770 remainder error R_1 (Lagrange mean-value form) induced in a single cycle is:

$$771 \quad F(\hat{x}_{n-1}+z\sqrt{P_n};u_n) - F(\hat{x}_{n-1}) - \frac{\partial F(x;u_n)}{\partial x} z\sqrt{P_n} =$$

$$772 \quad R_1(\hat{x}_{n-1}+z\sqrt{P_n}) = \frac{\partial^2 F(\xi_L;u_n)}{\partial \xi_L^2} \frac{(z\sqrt{P_n})^2}{2} \quad \text{for } \xi_L \in [\hat{x}_{n-1}-|z|\sqrt{P_n}, \hat{x}_{n-1}+|z|\sqrt{P_n}] \quad (B1)$$

$$773 \quad = \left(\frac{0.4407\text{m}}{\text{AOD}_n+9.73\text{m}} \left(\frac{1}{629.9} \right) - \left(\frac{1.385}{8464} \right) \log_{10} \left(\frac{1.893*10^{15}\text{ppm}}{[\text{CO}_2]_n} \right) \left(\frac{\xi_L}{8464\text{K}} \right)^{0.385} \right) \frac{z^2 P_n}{2} \quad (B2)$$

$$774 \quad -0.000284z^2 P_n < R_1(\hat{x}_{n-1}+z\sqrt{P_n}) < -0.000246z^2 P_n \quad (B3)$$

$$775 \quad \frac{|R_1(\hat{x}_{n-1}+z\sqrt{P_n})|}{|z|\sqrt{P_n}} < 0.000284|z|*(0.0307) < |z|*10^{-5} \quad (B4)$$

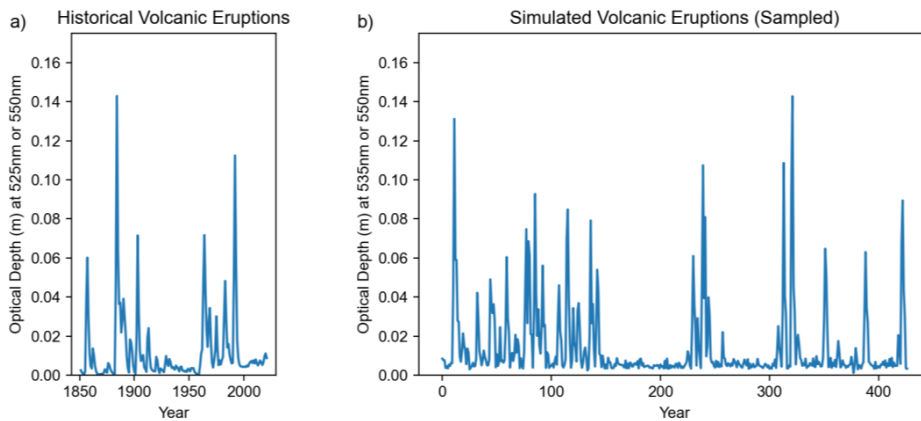
776 This means that even if the error accumulates in the same direction in each cycle of the EKF,
 777 over the 171 year timeseries all probability masses that are within $|z| < 5.85$ standard
 778 deviations will have an error of $< 1\%$, compared to a particle method such as the Unscented
 779 Kalman Filter. (Julier and Uhlmann 1997; Wan and Van Der Merwe 2000)

780

781 **Appendix C: Generation of Volcanic Eruption Samplings**

782 As can be appreciated in Fig. C1a, long periods of no major volcanic eruptions (for
 783 instance 1935-1960) alternated with periods of many eruptions occurring in rapid succession
 784 (1883-1914, 1960-1994). Perhaps this observed pattern has some relation to magma or
 785 tectonic dynamics, but it prevented one Poisson distribution from describing the data well.

786



787 Fig. C1: Comparison of Historical Volcanic Eruptions (C1a) with Simulated Volcanic
 788 Eruptions (C1b), generated from a combination of several probability distributions.

789

790 Eruptions that occurred within 3 years were indistinguishable in the historical dataset,
791 so the minimum time interval between simulated volcanic eruptions was 2.6 years plus a
792 sample (Table C1) from the exponential mixture model i_n (Okada, Yamanishi et al. 2020).
793 These intervals were rounded to integers. Similarly, the size of each volcanic eruption h_n was
794 approximated using another shifted exponential distribution. The preceding year and two
795 years following the eruption peak were positive fractions of the maximum aerosol optical
796 depth, with gaussian blur. Similarly, non-volcanic years were positive gaussian noise (Table
797 C2). Fig. C1b shows a sample from this combined generating function.

Exponential Distribution	Random Var.	Scale (units)	P(choose) (if mixture)
Interval Between: $\text{round}(i_{n,0} + 2.6)$	$i_{n,0} \sim \text{Exp}$	2.263 (years)	88.9%
Interval Between: $\text{round}(i_{n,1} + 2.6)$	$i_{n,0} \sim \text{Exp}$	24.2 (years)	11.1%
Peak Size: $\text{AOD}_n = h_n + 0.0082$	$h_n \sim \text{Exp}$	0.0339 (m)	

798 Table C1. Exponential Parameters of Volcano Generating Function. This generating function
799 starts with a list of zero values for all AOD_n , and first samples several of these n years to be
800 major volcanic eruptions. “Interval Between” refers to the interval in years between two
801 successive major volcanic eruptions.
802

Gaussian Distribution	Random Var.	Mean μ (units)	Std Dev σ
Pre-Peak: $\text{AOD}_{n-1} = a_{-1} * E_n$	$a_{-1} \sim \text{Norm} > 0$	0.51	0.25
Post-Peak 1: $\text{AOD}_{n+1} = a_1 * E_n$	$a_1 \sim \text{Norm} > 0$	0.61	0.16
Post-Peak 2: $\text{AOD}_{n+2} = a_2 * E_n$	$a_2 \sim \text{Norm} > 0$	0.32	0.16
Other Years: $\text{AOD}_n = a_0$	$a_0 \sim \text{Norm} > 0$	0.00371 (m)	0.00286 (m)

803 Table C2. Gaussian Parameters of Volcano Generating Function. These distributions are
804 sampled after the major eruptions have already been filled in by the exponential distributions
805 in Table 1.
806

- 808 Annan, J. D., J. C. Hargreaves, N. R. Edwards and R. Marsh (2005). "Parameter estimation in
809 an intermediate complexity earth system model using an ensemble Kalman filter." *Ocean*
810 *Modelling* **8**(1): 135-154 DOI: <https://doi.org/10.1016/j.ocemod.2003.12.004>.
- 811 Benhamou, E. (2018). "Kalman filter demystified: from intuition to probabilistic graphical
812 model to real case in financial markets." *arXiv e-prints Statistical Finance (q-*
813 *fin.ST)*(arXiv:1811.11618) DOI: <https://doi.org/10.48550/arXiv.1811.11618>.
- 814 Boltzmann, L. (1884). "Ableitung des Stefan'schen Gesetzes, betreffend die Abhängigkeit der
815 Wärmestrahlung von der Temperatur aus der electromagnetischen Lichttheorie." *Annalen der*
816 *Physik* **258**(6): 291-294 DOI: <https://doi.org/10.1002/andp.18842580616>.
- 817 Bouttier, F. (1996). *Application of Kalman filtering to numerical weather prediction.*
818 Workshop on non-linear aspects of data assimilation, Shinfield Park, Reading, ECMWF.
- 819 Budyko, M. I. (1969). "The effect of solar radiation variations on the climate of the Earth."
820 *Tellus* **21**(5): 611-619 DOI: 10.3402/tellusa.v21i5.10109.
- 821 Buizza, R., M. Milleer and T. N. Palmer (1999). "Stochastic representation of model
822 uncertainties in the ECMWF ensemble prediction system." *Quarterly Journal of the Royal*
823 *Meteorological Society* **125**(560): 2887-2908 DOI: <https://doi.org/10.1002/qj.49712556006>.
- 824 Carré, M., J. P. Sachs, J. M. Wallace and C. Favier (2012). "Exploring errors in paleoclimate
825 proxy reconstructions using Monte Carlo simulations: paleotemperature from mollusk and
826 coral geochemistry." *Clim. Past* **8**(2): 433-450 DOI: 10.5194/cp-8-433-2012.
- 827 Edwards, T. L., S. Nowicki, B. Marzeion, R. Hock, H. Goelzer, H. Seroussi, N. C. Jourdain,
828 D. A. Slater, F. E. Turner, C. J. Smith, C. M. McKenna, E. Simon, A. Abe-Ouchi, J. M.
829 Gregory, E. Larour, W. H. Lipscomb, A. J. Payne, A. Shepherd, C. Agosta, P. Alexander, T.
830 Albrecht, B. Anderson, X. Asay-Davis, A. Aschwanden, A. Barthel, A. Bliss, R. Calov, C.
831 Chambers, N. Champollion, Y. Choi, R. Cullather, J. Cuzzone, C. Dumas, D. Felikson, X.
832 Fettweis, K. Fujita, B. K. Galton-Fenzi, R. Gladstone, N. R. Golledge, R. Greve, T.
833 Hattermann, M. J. Hoffman, A. Humbert, M. Huss, P. Huybrechts, W. Immerzeel, T. Kleiner,
834 P. Kraaijenbrink, S. Le clec'h, V. Lee, G. R. Leguy, C. M. Little, D. P. Lowry, J.-H. Malles,
835 D. F. Martin, F. Maussion, M. Morlighem, J. F. O'Neill, I. Nias, F. Pattyn, T. Pelle, S. F.
836 Price, A. Quiquet, V. Radić, R. Reese, D. R. Rounce, M. Rückamp, A. Sakai, C. Shafer, N.-J.
837 Schlegel, S. Shannon, R. S. Smith, F. Straneo, S. Sun, L. Tarasov, L. D. Trusel, J. Van
838 Breedam, R. van de Wal, M. van den Broeke, R. Winkelmann, H. Zekollari, C. Zhao, T.
839 Zhang and T. Zwinger (2021). "Projected land ice contributions to twenty-first-century sea
840 level rise." *Nature* **593**(7857): 74-82 DOI: 10.1038/s41586-021-03302-y.
- 841 Emile-Geay, J., N. P. McKay, D. S. Kaufman, L. von Gunten, J. Wang, K. J. Anchukaitis, N.
842 J. Abram, J. A. Addison, M. A. J. Curran, M. N. Evans, B. J. Henley, Z. Hao, B. Martrat, H.
843 V. McGregor, R. Neukom, G. T. Pederson, B. Stenni, K. Thirumalai, J. P. Werner, C. Xu, D.
844 V. Divine, B. C. Dixon, J. Gergis, I. A. Mundo, T. Nakatsuka, S. J. Phipps, C. C. Routson, E.
845 J. Steig, J. E. Tierney, J. J. Tyler, K. J. Allen, N. A. N. Bertler, J. Björklund, B. M. Chase,
846 M.-T. Chen, E. Cook, R. de Jong, K. L. DeLong, D. A. Dixon, A. A. Ekaykin, V. Ersek, H.
847 L. Filipsson, P. Francus, M. B. Freund, M. Frezzotti, N. P. Gaire, K. Gajewski, Q. Ge, H.
848 Goosse, A. Gornostaeva, M. Grosjean, K. Horiuchi, A. Hormes, K. Husum, E. Isaksson, S.
849 Kandasamy, K. Kawamura, K. H. Kilbourne, N. Koç, G. Leduc, H. W. Linderholm, A. M.
850 Lorrey, V. Mikhalenko, P. G. Mortyn, H. Motoyama, A. D. Moy, R. Mulvaney, P. M. Munz,
851 D. J. Nash, H. Oerter, T. Opel, A. J. Orsi, D. V. Ovchinnikov, T. J. Porter, H. A. Roop, C.
852 Saenger, M. Sano, D. Sauchyn, K. M. Saunders, M.-S. Seidenkrantz, M. Severi, X. Shao, M.-

853 A. Sicre, M. Sigl, K. Sinclair, S. St. George, J.-M. St. Jacques, M. Thamban, U. Kuwar
854 Thapa, E. R. Thomas, C. Turney, R. Uemura, A. E. Viau, D. O. Vladimirova, E. R. Wahl, J.
855 W. C. White, Z. Yu, J. Zinke and P. A. k. Consortium (2017). "A global multiproxy database
856 for temperature reconstructions of the Common Era." Scientific Data **4**(1): 170088 DOI:
857 10.1038/sdata.2017.88.

858 Feng, R., B. L. Otto-Bliesner, E. C. Brady and N. Rosenbloom (2020). "Increased Climate
859 Response and Earth System Sensitivity From CCSM4 to CESM2 in Mid-Pliocene
860 Simulations." Journal of Advances in Modeling Earth Systems **12**(8): e2019MS002033 DOI:
861 <https://doi.org/10.1029/2019MS002033>.

862 Filar, J. A., P. S. Gaertner and M. A. Janssen (1996). An Application of Optimization to the
863 Problem of Climate Change. State of the Art in Global Optimization: Computational Methods
864 and Applications. C. A. Floudas and P. M. Pardalos. Boston, MA, Springer US: 475-498
865 DOI: 10.1007/978-1-4613-3437-8_29.

866 Forster, P., T. Storelvmo, K. Armour, W. Collins, J. L. Dufresne, D. Frame, D. J. Lunt, T.
867 Mauritsen, M. D. Palmer, M. Watanabe, M. Wild and H. Zhang (2021). The Earth's Energy
868 Budget, Climate Feedbacks, and Climate Sensitivity. Climate Change 2021: The Physical
869 Science Basis. Contribution of Working Group I to the Sixth Assessment Report of the
870 Intergovernmental Panel on Climate Change. V. Masson-Delmotte, P. Zhai, A. Pirani et al.
871 Cambridge, United Kingdom and New York, NY, USA, Cambridge University Press: 923–
872 1054 DOI: 10.1017/9781009157896.009.

873 Fujino, J., R. Nair, M. Kainuma, T. Masui and Y. Matsuoka (2006). "Multi-gas Mitigation
874 Analysis on Stabilization Scenarios Using Aim Global Model." The Energy Journal **27**: 343-
875 353.

876 Gettelman, A., C. Hannay, J. T. Bacmeister, R. B. Neale, A. G. Pendergrass, G. Danabasoglu,
877 J. F. Lamarque, J. T. Fasullo, D. A. Bailey, D. M. Lawrence and M. J. Mills (2019). "High
878 Climate Sensitivity in the Community Earth System Model Version 2 (CESM2)."
879 Geophysical Research Letters **46**(14): 8329-8337 DOI:
880 <https://doi.org/10.1029/2019GL083978>.

881 Grewal, M. S. and A. P. Andrews (2001). Kalman Filtering: Theory and Practice Using
882 MATLAB, Wiley.

883 Gulev, S. K., P. W. Thorne, J. Ahn, F. J. Dentener, C. M. Domingues, S. Gerland, D. Gong,
884 D. S. Kaufman, H. C. Nnamchi, J. Quaas, J. A. Rivera, S. Sathyendranath, S. L. Smith, B.
885 Trewin, K. von Schuckmann and R. S. Vose (2021). Changing State of the Climate System.
886 Climate Change 2021: The Physical Science Basis. Contribution of Working Group I to the
887 Sixth Assessment Report of the Intergovernmental Panel on Climate Change. V. Masson-
888 Delmotte, P. Zhai, A. Pirani et al. Cambridge, United Kingdom and New York, NY, USA,
889 Cambridge University Press: 287–422 DOI: 10.1017/9781009157896.004.

890 Guttman, N. B. (1989). "Statistical Descriptors of Climate." Bulletin of the American
891 Meteorological Society **70**(6): 602-607 DOI: 10.1175/1520-
892 0477(1989)070<0602:SDOC>2.0.CO;2.

893 Harshvardhan and M. D. King (1993). "Comparative Accuracy of Diffuse Radiative
894 Properties Computed Using Selected Multiple Scattering Approximations." Journal of the
895 Atmospheric Sciences **50**(2): 247-259 DOI: 10.1175/1520-
896 0469(1993)050<0247:caodrp>2.0.co;2.

897 Hijioaka, Y., Y. Matsuoka, H. Nishimoto, T. Masui and M. Kainuma (2008). "Global GHG
898 Emission Scenarios Under GHG Cconcentration Stabilization Targets." Journal of global
899 environment engineering **13**: 97-108.

900 Hu, S. and A. V. Fedorov (2017). "The extreme El Niño of 2015-2016 and the end of global
901 warming hiatus." Geophysical Research Letters **44**(8): 3816-3824 DOI:
902 10.1002/2017GL072908.

903 Jones, P. D. and C. Harpham (2013). "Estimation of the absolute surface air temperature of
904 the Earth." Journal of Geophysical Research: Atmospheres **118**(8): 3213-3217 DOI:
905 <https://doi.org/10.1002/jgrd.50359>.

906 Julier, S. J. and J. K. Uhlmann (1997). New extension of the Kalman filter to nonlinear
907 systems. Proc.SPIE DOI: 10.1117/12.280797.

908 Kalman, R. E. (1960). "A New Approach to Linear Filtering and Prediction Problems."
909 Journal of Basic Engineering **82**(1): 35-45 DOI: 10.1115/1.3662552.

910 Kalman, R. E. and R. S. Bucy (1961). "New Results in Linear Filtering and Prediction
911 Theory." Journal of Basic Engineering **83**(1): 95-108 DOI: 10.1115/1.3658902.

912 Kaufman, D., N. McKay, C. Routson, M. Erb, B. Davis, O. Heiri, S. Jaccard, J. Tierney, C.
913 Dätwyler, Y. Axford, T. Brussel, O. Cartapanis, B. Chase, A. Dawson, A. De Vernal, S.
914 Engels, L. Jonkers, J. Marsicek, P. Moffa-Sánchez, C. Morrill, A. Orsi, K. Rehfeld, K.
915 Saunders, P. S. Sommer, E. Thomas, M. Tonello, M. Tóth, R. Vachula, A. Andreev, S.
916 Bertrand, B. Biskaborn, M. Bringué, S. Brooks, M. Caniupán, M. Chevalier, L. Cwynar, J.
917 Emile-Geay, J. Fegyveresi, A. Feurdean, W. Finsinger, M.-C. Fortin, L. Foster, M. Fox, K.
918 Gajewski, M. Grosjean, S. Hausmann, M. Heinrichs, N. Holmes, B. Ilyashuk, E. Ilyashuk, S.
919 Juggins, D. Khider, K. Koinig, P. Langdon, I. Larocque-Tobler, J. Li, A. Lotter, T. Luoto, A.
920 Mackay, E. Magyari, S. Malevich, B. Mark, J. Massaferró, V. Montade, L. Nazarova, E.
921 Novenko, P. Pařil, E. Pearson, M. Peros, R. Pienitz, M. Plóciennik, D. Porinchu, A. Potito, A.
922 Rees, S. Reinemann, S. Roberts, N. Rolland, S. Salonen, A. Self, H. Seppä, S. Shala, J.-M.
923 St-Jacques, B. Stenni, L. Syrykh, P. Tarrats, K. Taylor, V. Van Den Bos, G. Velle, E. Wahl,
924 I. Walker, J. Wilmshurst, E. Zhang and S. Zhilich (2020). "A global database of Holocene
925 paleotemperature records." Scientific Data **7**(1) DOI: 10.1038/s41597-020-0445-3.

926 Kirtman, B., S. B. Power, A. J. Adedoyin, G. J. Boer, R. Bojariu, I. Camilloni, F. Doblas-
927 Reyes, A. M. Fiore, M. Kimoto, G. Meehl, M. Prather, A. Sarr, C. Schär, R. Sutton, G. J. van
928 Oldenborgh, G. Vecchi and H. J. Wang (2013). Near-term climate change. Projections and
929 predictability, Cambridge University Press. **9781107057999**: 953-1028 DOI:
930 10.1017/CBO9781107415324.023.

931 Kopp, G. and J. L. Lean (2011). "A new, lower value of total solar irradiance: Evidence and
932 climate significance." Geophysical Research Letters **38**(1) DOI:
933 <https://doi.org/10.1029/2010GL045777>.

934 Kravitz, B., D. G. MacMartin, H. Wang and P. J. Rasch (2016). "Geoengineering as a design
935 problem." Earth System Dynamics **7**(2): 469-497 DOI: 10.5194/esd-7-469-2016.

936 Kravitz, B., P. J. Rasch, H. Wang, A. Robock, C. Gabriel, O. Boucher, J. N. S. Cole, J.
937 Haywood, D. Ji, A. Jones, A. Lenton, J. C. Moore, H. Muri, U. Niemeier, S. Phipps, H.
938 Schmidt, S. Watanabe, S. Yang and J. H. Yoon (2018). "The climate effects of increasing
939 ocean albedo: an idealized representation of solar geoengineering." Atmos. Chem. Phys.
940 **18**(17): 13097-13113 DOI: 10.5194/acp-18-13097-2018.

941 Lacey, T. (1998). "Tutorial: The kalman filter." Computer Vision.

942 Lauritzen, S. L. (1981). "Time Series Analysis in 1880: A Discussion of Contributions Made
943 by T.N. Thiele." International Statistical Review / Revue Internationale de Statistique **49**(3):
944 319-331 DOI: 10.2307/1402616.

945 Lauritzen, S. L. and T. N. Thiele (2002). Thiele: Pioneer in Statistics, Oxford University
946 Press.

947 Lee, J. H. and N. L. Ricker (1994). "Extended Kalman Filter Based Nonlinear Model
948 Predictive Control." Industrial and Engineering Chemistry Research **33**(6): 1530-1541 DOI:
949 10.1021/ie00030a013.

950 Lee, J. Y., J. Marotzke, G. Bala, L. Cao, S. Corti, J. P. Dunne, F. Engelbrecht, E. Fischer, J.
951 C. Fyfe, C. Jones, A. Maycock, J. Mutemi, O. Ndiaye, S. Panickal and T. Zhou (2021).
952 Future Global Climate: Scenario-Based Projections and Near-Term Information. Climate
953 Change 2021: The Physical Science Basis. Contribution of Working Group I to the Sixth
954 Assessment Report of the Intergovernmental Panel on Climate Change. V. Masson-Delmotte,
955 P. Zhai, A. Pirani et al. Cambridge, United Kingdom and New York, NY, USA, Cambridge
956 University Press: 553–672 DOI: 10.1017/9781009157896.006.

957 Lenssen, N. J. L., G. A. Schmidt, J. E. Hansen, M. J. Menne, A. Persin, R. Ruedy and D.
958 Zyss (2019). "Improvements in the GISTEMP Uncertainty Model." Journal of Geophysical
959 Research: Atmospheres **124**(12): 6307-6326 DOI: <https://doi.org/10.1029/2018JD029522>.

960 Livezey, R. E., K. Y. Vinnikov, M. M. Timofeyeva, R. Tinker and H. M. van den Dool
961 (2007). "Estimation and Extrapolation of Climate Normals and Climatic Trends." Journal of
962 Applied Meteorology and Climatology **46**(11): 1759-1776 DOI: 10.1175/2007JAMC1666.1.

963 Loeb, N. G., B. A. Wielicki, D. R. Doelling, G. L. Smith, D. F. Keyes, S. Kato, N. Manalo-
964 Smith and T. Wong (2009). "Toward Optimal Closure of the Earth's Top-of-Atmosphere
965 Radiation Budget." Journal of Climate **22**(3): 748-766 DOI: 10.1175/2008jcli2637.1.

966 MacMartin, D. G., B. Kravitz and D. W. Keith (2014). Geoengineering: The world's largest
967 control problem. 2014 American Control Conference, IEEE.

968 Mann, M. E. (2008). "Smoothing of climate time series revisited." Geophysical Research
969 Letters **35**(16) DOI: <https://doi.org/10.1029/2008GL034716>.

970 Marotzke, J. and P. M. Forster (2015). "Forcing, feedback and internal variability in global
971 temperature trends." Nature **517**(7536): 565-570 DOI: 10.1038/nature14117.

972 McClelland, H. L. O., I. Halevy, D. A. Wolf-Gladrow, D. Evans and A. S. Bradley (2021).
973 "Statistical Uncertainty in Paleoclimate Proxy Reconstructions." Geophysical Research
974 Letters **48**(15): e2021GL092773 DOI: <https://doi.org/10.1029/2021GL092773>.

975 Meehl, G. A., R. Moss, K. E. Taylor, V. Eyring, R. J. Stouffer, S. Bony and B. Stevens
976 (2014). "Climate Model Intercomparisons: Preparing for the Next Phase." Eos, Transactions
977 American Geophysical Union **95**(9): 77-78 DOI: <https://doi.org/10.1002/2014EO090001>.

978 Merchant, C. J., O. Embury, C. E. Bulgin, T. Block, G. K. Corlett, E. Fiedler, S. A. Good, J.
979 Mittaz, N. A. Rayner, D. Berry, S. Eastwood, M. Taylor, Y. Tsushima, A. Waterfall, R.
980 Wilson and C. Donlon (2019). "Satellite-based time-series of sea-surface temperature since
981 1981 for climate applications." Scientific Data **6**(1) DOI: 10.1038/s41597-019-0236-x.

982 Miller, R. N. (1996). Introduction to the Kalman filter. Seminar on Data Assimilation, 2-6
983 September 1996, Shinfield Park, Reading, ECMWF.

984 Morice, C. P., J. J. Kennedy, N. A. Rayner and P. D. Jones (2012). "Quantifying uncertainties
985 in global and regional temperature change using an ensemble of observational estimates: The

- 986 HadCRUT4 data set." Journal of Geophysical Research: Atmospheres **117**(D8) DOI:
987 <https://doi.org/10.1029/2011JD017187>.
- 988 Morice, C. P., J. J. Kennedy, N. A. Rayner, J. P. Winn, E. Hogan, R. E. Killick, R. J. H.
989 Dunn, T. J. Osborn, P. D. Jones and I. R. Simpson (2021). "An Updated Assessment of Near-
990 Surface Temperature Change From 1850: The HadCRUT5 Data Set." Journal of Geophysical
991 Research: Atmospheres **126**(3): e2019JD032361 DOI:
992 <https://doi.org/10.1029/2019JD032361>.
- 993 Myers, M. A. and R. H. Luecke (1991). "Process control applications of an extended Kalman
994 filter algorithm." Computers & Chemical Engineering **15**(12): 853-857 DOI:
995 [https://doi.org/10.1016/0098-1354\(91\)80030-Y](https://doi.org/10.1016/0098-1354(91)80030-Y).
- 996 Nasa/Larc/Sd/Asdc (2018). Global Space-based Stratospheric Aerosol Climatology Version
997 2.0.
- 998 Ogorek, B. (2019) "Yet Another Kalman Filter Explanation Article." Towards Data Science.
- 999 Okada, M., K. Yamanishi and N. Masuda (2020). "Long-tailed distributions of inter-event
1000 times as mixtures of exponential distributions." Royal Society Open Science **7**: 191643 DOI:
1001 10.1098/rsos.191643.
- 1002 Papale, P. (2018). "Global time-size distribution of volcanic eruptions on Earth." Scientific
1003 Reports **8**(1): 6838 DOI: 10.1038/s41598-018-25286-y.
- 1004 Pielke Jr, R., M. G. Burgess and J. Ritchie (2022). "Plausible 2005–2050 emissions scenarios
1005 project between 2 °C and 3 °C of warming by 2100." Environmental Research Letters **17**(2):
1006 024027 DOI: 10.1088/1748-9326/ac4ebf.
- 1007 Rauch, H. E., F. Tung and C. T. Striebel (1965). "Maximum likelihood estimates of linear
1008 dynamic systems." AIAA Journal **3**(8): 1445-1450 DOI: 10.2514/3.3166.
- 1009 Rodgers, K. B., S. S. Lee, N. Rosenbloom, A. Timmermann, G. Danabasoglu, C. Deser, J.
1010 Edwards, J. E. Kim, I. R. Simpson, K. Stein, M. F. Stuecker, R. Yamaguchi, T. Bódai, E. S.
1011 Chung, L. Huang, W. M. Kim, J. F. Lamarque, D. L. Lombardozzi, W. R. Wieder and S. G.
1012 Yeager (2021). "Ubiquity of human-induced changes in climate variability." Earth Syst.
1013 Dynam. **12**(4): 1393-1411 DOI: 10.5194/esd-12-1393-2021.
- 1014 Ruggieri, E. and M. Antonellis (2016). "An exact approach to Bayesian sequential change
1015 point detection." Computational Statistics & Data Analysis **97**: 71-86 DOI:
1016 <https://doi.org/10.1016/j.csda.2015.11.010>.
- 1017 Särkkä, S. (2013). Bayesian Filtering and Smoothing, Cambridge University Press.
- 1018 Sato, M., J. E. Hansen, M. P. McCormick and J. B. Pollack (1993). "Stratospheric aerosol
1019 optical depths, 1850-1990." J. Geophys. Res. **98**: 22987-22994 DOI: 10.1029/93JD02553.
- 1020 Schmidt, S. F. (1981). "The Kalman filter - Its recognition and development for aerospace
1021 applications." Journal of Guidance and Control **4**(1): 4-7 DOI: 10.2514/3.19713.
- 1022 Schwartz, S. E. (2007). "Heat capacity, time constant, and sensitivity of Earth's climate
1023 system." Journal of Geophysical Research **112**(D24): D24S05-D24S05 DOI:
1024 10.1029/2007JD008746.
- 1025 Schwartz, S. E., n. Harshvardhan and C. M. Benkovitz (2002). "Influence of anthropogenic
1026 aerosol on cloud optical depth and albedo shown by satellite measurements and chemical
1027 transport modeling." Proceedings of the National Academy of Sciences **99**(4): 1784-1789
1028 DOI: 10.1073/pnas.261712099.